ORIGINAL PAPER

High-pressure melting in metapelites of a 2 Ga old subducted oceanic crust (Usagaran belt, Tanzania): implications from melt inclusions, fluid inclusions and thermodynamic modelling

Petra Herms[1] · Peter Raase[1] · Christopher Giehl[1,2] · László E. Aradi[3,4] · Tobias Fußwinkel[5] · Arno Rohrbach[6] · Andreas Möller[7]

Abstract
Investigation of polymineralic melt inclusions preserved in garnet of eclogite-facies metapelites of the Usagaran belt, Tanzania, is of particular importance as these metapelites, intercalated in oceanic metabasites, document the rare case of partial melting at high temperatures in a subducted oceanic crust. With an age of 2 Ga the rocks represent one of the oldest oceanic crusts and confirm a subduction process already at Paleoproterozoic times. Partial melting probably was initiated by dehydration melting under the presence of a CO_2-rich fluid phase. The melt is preserved in siliceous polymineralic inclusions, while CO_2 locally reacted with the garnet host to form dolomite-quartz-kyanite inclusions. During this reaction, the REE spectrum of garnet is adopted by the dolomite. Furthermore, graphite inclusions in garnet must have precipitated from the CO_2 fluid by reduction. The highly ordered graphite structure indicates a formation temperature of at least 700 °C. Rehomogenization experiments of the siliceous polymineralic inclusions yield a homogeneous melt of rhyolitic, peraluminous composition. Thermodynamic modelling enables to deduce a P–T path in accordance with high P–T conditions (minimum 2.0 GPa, 900 °C) where a partial melt formed due to phengite breakdown leading to the preserved peak mineral assemblage garnet, alkali feldspar, kyanite, quartz and rutile. A very fast uplift of the oceanic crustal rocks can be deduced from the occurrence of very finely exsolved metastable ternary feldspar and from the preserved prograde zoning in garnet.

Communicated by Othmar Müntener.

✉ Petra Herms
petra.herms@ifg.uni-kiel.de

1 Department of Geosciences, University of Kiel, 24118 Kiel, Germany

2 Anton Paar Germany GmbH, 73760 Ostfildern, Germany

3 Lithosphere Fluid Research Laboratory, Institute of Geography and Earth Sciences, Eötvös Loránd University, 1117 Budapest, Hungary

4 Present Address: Department of Geosciences, University of Padua, 35131 Padua, Italy

5 Institute of Applied Mineralogy and Economic Geology, RWTH Aachen University, 52062 Aachen, Germany

6 Department of Mineralogy, University of Münster, 48149 Münster, Germany

7 Department of Geology, The University of Kansas, 1475 Jayhawk Blvd, Lawrence, KS 66045, USA

Introduction

To recognize former melts in rock sequences in which otherwise no evidence for partial melting or anatexis are obvious, the investigation of polymineralic inclusions, preserving primary melts, is the most valuable tool. Melt inclusions provide information about the composition of primary melts, the P–T conditions of melting, and the processes of melt production. Furthermore, melts play a role in geodynamic processes and they influence, e.g. the exhumation rate in orogenic terrains (Hermann et al. 2001). Anatexis or partial melting of the lower continental crust indicated by polymineralic inclusions has been described by, e.g. Cesare et al. (2009, 2015), Ferrero et al. (2012, 2014), Barich et al. (2014), Bartoli et al. (2016), Tacchetto et al. (2018) and Carvalho et al. (2019) for different terranes. In subducted continental crust, partial melting is indicated by polymineralic inclusions, which preserve the

primary melt or a dense supercritical fluid (e.g. Stöckert et al. 2001; Ferrando et al. 2005; Korsakov and Hermann 2006; Lang and Gilotti 2007; Ferrero et al. 2015; Gao et al. 2017; Deng et al. 2018). Melting during subduction of the continental crust may occur at peak conditions or during the decompressional uplift path. Lang and Gilotti (2007) conclude that melting occurred during a steep decompression path, but with only a small volume percentage of melt. For the Western Gneiss region Labrousse et al. (2011) show that partial melting of the continental crust occurred in the UHP as well as in the HP domains at their respectively peak pressures. The existence of partial melts at such high-grade conditions let Labrousse et al. (2011) conclude that exhumation of the continental crust has been initiated by partial melting. Even a small amount of partial melt should induce a weakening of the rocks, accelerating the uplift.

In contrast to continental subduction, subducted oceanic rocks generally remain cooler even at UHP conditions, they rarely show signs of partial melting and are rapidly exhumed mainly through subduction channels (Gerya et al. 2002). Polymineralic inclusions described by Frezzotti et al. (2011) in oceanic rocks subducted to UHP crystallized from a solute-rich fluid instead of a melt. Only from few Paleoproterozoic or Archean oceanic rocks, a high-temperature subduction has been reported, however, without observing partial melting (Houketchang Bouyo et al. 2019; Ning et al. 2022).

As investigations on melt inclusions in oceanic crustal rocks have not been reported to our knowledge, the discovery of polymineralic, former melt inclusions in Proterozoic eclogite-facies rocks is of special interest, because the melt inclusions are a strong indication of high temperatures during subduction. These rocks are some of the oldest subducted oceanic crusts (2 Ga, Möller et al. 1995; Collins et al. 2004; Tamblyn et al. 2021) and provide evidence for the operation of plate tectonic processes during the Paleoproterozoic. The polymineralic inclusions occur in garnet porphyroblasts in metapelites interlayered between metabasites of mid-ocean ridge affinity from Yalumba Hill, Usagaran belt, Tanzania.

In this paper, we apply various techniques to one sample of restitic metapelite containing polymineralic inclusions in garnet porphyroblasts. Remelting experiments on polymineralic inclusions have been combined with thermodynamic modelling using the melt composition to derive the P–T conditions of melt entrapment and to constrain the subsequent decompression path, considering both stable and metastable mineral phases observed along this path. Raman spectroscopy is used to determine the composition of fluid inclusions and of secondary minerals inside fluid and polymineralic inclusions, to determine the composition of the fluid present during the subduction process. Trace element analyses on carbonate-bearing inclusions are used to investigate the origin of these inclusions.

Geological background

The eclogite-facies metapelites of Yalumba Hill belong to the Paleoproterozoic Usagaran belt in Tanzania bordered by the Archean Tanzania craton (crust formation at about 2.7 Ga, Möller et al. 1998) to the west and an Archean continental crustal province (e.g. Möller et al. 1998; Maboko 2000) with a Pan-African (0.61–0.65 Ga) amphibolite to granulite facies metamorphic overprint to the east. The metapelites are intercalated with km-scale eclogite-facies metabasites and marine marbles (Meinhold and Ott 1993; Möller et al. 1995; Collins et al. 2004; Tamblyn et al. 2021; Brown et al. 2020). Geochemical investigations indicate a MORB-type mantle source for the mafic eclogite-facies rocks (Möller et al. 1995). This implies that the whole lithology represents a subduction-related ancient oceanic crust, where metapelitic and mafic gneisses were coevally subducted to great depth at high P–T conditions (Möller et al. 1995; Brown et al. 2020). Boniface and Tsujimori (2019) assign a back-arc MORB origin to greenschist-facies pillow basalts from the adjacent Konse Group, which they regard as coeval to the Usagaran eclogite mafic units. U–Pb geochronology on both Usagaran metapelites (monazite) and metabasites (titanite) gives an age of 2 Ga for the peak of metamorphism, confirmed by the 1991 ± 2 Ma U–Pb zircon age of a cross-cutting pegmatite (Collins et al. 2004). This unit therefore represents one of the oldest known subduction-related pieces of oceanic crust (Möller et al. 1995), together with occurrences of Paleoproterozoic subduction-related eclogites in Russia, Asia, North America and Africa (see recent compilations by Boniface and Tsujimori (2021) and Tamblyn et al. (2021)).

Methods

Electron microprobe

Major elements were analysed using a JEOL Superprobe JXA-8900R electron microprobe (EMP, University of Kiel, Germany) at an accelerating voltage of 15 kV and a beam current of 15 nA for silicate minerals, 15 kV and 15 nA for polymineralic inclusions in garnet and 15 kV and 10 nA for carbonates. For EMP analyses on silicates, a focused beam (with beam size 1 μm) was used except for feldspars and carbonates where the beam diameter was defocused to 5 μm. The counting time of each element during the mineral analysis was 15 s on the peak and 7 s on the background. X-ray compositional maps were obtained, using an accelerating voltage of 15 kV, a beam current of

40 nA and a dwell time for garnet porphyroblasts of 80 ms and for the polymineralic inclusions of 50–60 ms.

EMP analyses of glass generally bear the problem of Na loss during the measurements. Therefore, we always used a defocused beam diameter of 5 μm and changed the beam current and the counting rate. For Na analyses a beam current of 3 nA as well as 1 nA was chosen and the counting time on the peak was 50 s, and 25 s on the background, for all other elements the counting time on the peak was 75 s, and 35 s on the background, except for Mn where the counting time on the peak was 75 s, and 25 s on the background. Measurements with the same setup and configuration on an obsidian reference material confirmed element concentrations and totals.

Micro-Raman spectroscopic analyses

Micro-Raman spectroscopic analyses were done at the Research and Industrial Relations Center (RIRC) of the Faculty of Science, Eötvös Loránd University, Budapest, using a confocal HORIBA LabRAM HR800 high resolution spectrometer with a Nd:YAG laser ($\lambda = 532$ nm) excitation and 600 grooves/mm optical grating for mapping, 1800 grooves/mm optical grating for spot measurements, and a 50 μm confocal hole. An OLYMPUS $100\times$ objective (NA = 0.9) was used to focus the laser on the inclusions. Spot Raman maps were recorded from carbonate-rich polymineralic inclusions. Spot Raman spectra were collected with an acquisition time of 30–60 s and 2–8 accumulations for each spectrum. Spectra were acquired in the spectral range between 100 and 4000 cm^{-1}. The spectral resolution of measurements varied from 0.8 to 3.0 cm^{-1} for spot measurements, and from 2.4 to 3.0 cm^{-1} for maps.

To analyse additional components in aqueous fluid inclusions (e.g. $CaCl_2$, $MgCl_2$), a Linkam THMS600 heating/cooling stage was used to record Raman spectra at 22 °C, -100 °C and -190 °C. Raman data were processed using the LabSpec5 software. The online database of the RRUFF project (rruff.info; Lafuente et al. 2016) was used to identify the solid phases within the inclusions. The density (ρ) of CO_2 inclusions was calculated according to the method based on the distance (Δ) between the Fermi diad (two highest intensity Raman bands). The following 3rd order polynomial equation, that relates the CO_2 density to the splitting of the Fermi diad of CO_2 was used from Fall et al. (2011).

LA-ICP-MS analyses

The LA-ICP-MS analyses have been performed at RWTH Aachen University (Institute of Applied Mineralogy and Economic Geology) using a Coherent GeoLas HD 193 nm laser ablation system coupled to an Agilent 7900 s quadrupole ICP-MS with a high-sensitivity s-lens configuration using Pt skimmer and sampler cones. The machine was tuned daily to ensure high sensitivities throughout the entire mass range at low production rates of oxide and doubly-charged interferences (ThO/Th < 0.3% and Ca^{2+}/Ca < 0.2%), while maintaining stable ablation, transport, and ionization conditions (U/Th = 100 ± 2%). Ablations were performed at energy densities of 6 J/cm^2 and 10 Hz repetition rates. Spot sizes were adjusted to ensure complete ablation of the inclusion contents while minimizing contributions of the garnet matrix to the mixed signal.

The correction procedure for REE quantification in the inclusions involves several aspects. First, the signal of the carbonaceous inclusion is normalized to 100 wt% oxide components ($SiO_2 + TiO_2 + Al_2O_3 + Fe_2O_3 + FeO + MnO + MgO + CaO + Na_2O + K_2O + P_2O_5$). The $FeO/(Fe_2O_3 + FeO)$ ratio was assumed to be 1. In order to account for volatile components within the inclusions, the normalization results were scaled to the approximate volume percentage of non-volatile components of each inclusion. These volume proportions had been determined separately using image analysis of backscatter-electron images of each targeted inclusion. Second, the mixed signals of carbonaceous inclusion and host mineral were deconvoluted using two internal standards. The first internal standard is used to constrain the composition of the host mineral matrix. These values were taken from EMP analysis of garnet surrounding the inclusions. The second internal standard value is required to derive the relative proportions of carbonaceous inclusion and host mineral matrix in the mixed signal. For this second internal standard, major element compositional data of inclusion-hosted dolomite (EMP analyses) was used. With all these parameters fixed, the quantification was then carried out using the SILLS data reduction software package (Guillong et al. 2008). Standard reference material USGS GSE-1G was used as external standard for quantification of all melt inclusion compositions.

In order to verify the validity of the correction approach, different combinations of internal standards were tested. Three oxides (CaO, MgO or FeO) were tested as both first and second internal standards, resulting in nine different combinations. First, the reproduction of EMP analyses major element compositional data of the host mineral matrix (garnet) was tested for the different oxides. It was found that the best results were attained using CaO as first internal standard. Next, the reproduction of major element data of inclusion-hosted dolomite was tested using the different oxides as second internal standard. Again, CaO provided the best reproduction of major element compositional data. Based on these findings, the entire correction procedure for each carbonaceous inclusion was performed by using CaO as first and second internal standard.

Remelting experiments

For the rehomogenization of polymineralic inclusions, cylindrical samples (4 mm diameter, 7 mm length) containing several garnet crystals (2–3 mm in size) were drilled from sample T70G (Möller et al. 1995; Herms 2002). The rehomogenization experiments were performed with an end-loaded piston cylinder at high pressure and temperature. Four experiments were conducted at a constant pressure of 1.5 GPa and temperatures of 750, 850 and 900 °C (at the Department of Geosciences, CAU Kiel, Germany). The experiments were performed in a 1/2″ setup, where the drill cores were placed in a MgO cylinder, which in turn is enclosed within a graphite heater, a Pyrex glass sleeve and a pyrophyllite shell. The run duration of the experiments was 24 h at each temperature. Five additional experiments were conducted at a constant pressure of 2.5 GPa and temperatures of 950 °C (24 h), 1000 °C (6, 24, 48 h) and 1050 °C (24 h). These runs were done in end-loaded piston cylinder apparatus at the Institute of Mineralogy (University of Münster, Germany). Details of the experimental methods have been reported elsewhere (Grützner et al. 2017; Gervasoni et al. 2017). For the runs 1/2 inch talc-pyrex assemblies were used with inner parts of crushable alumina. At the end of each experiment, samples were quenched by turning off the power supply to below 200 °C within ~5 s. The drill cores were recovered, cut into thin slices and prepared for EMP analyses.

Thermodynamic modelling

Equilibrium phase diagrams were calculated with the Theriak–Domino software (De Capitani and Petrakakis 2010) with database tc55_Bt, which was recalculated by E. Duesterhöft (personal communication, 2022) with the database tc55 modified from Holland and Powell (1998). The activity-composition relationships of melts are modelled according to White et al. (2007). The solution models used are: Ti-biotite (Tajčmanová et al. 2009), phengite (Coggon and Holland 2002), garnet (White et al. 2007), plagioclase (Newton et al. 1980), ternary feldspar (Baldwin et al. 2005; Holland and Powell 2003), carbonate (Holland and Powell 2003).

Results

Petrography

The studied metapelite sample from Yalumba Hill (T70G, Fig. 1a) contains garnet porphyroblasts (2–3 mm) and smaller blasts of kyanite in a deformed matrix consisting of quartz, alkali feldspar and biotite. Rutile, apatite, sulfide

minerals, zircon, monazite, secondary dolomite and ilmenite are accessories. Kyanite blasts are rounded, often embayed, and deformed. Quartz occurs in bent ribbons with subgrain texture (Fig. 1b) and is locally recrystallized. Aggregates of fine-grained granoblastic orthoclase film perthite (Fig. 1b–d) contain relics of large perthitic alkali feldspar grains. Reddish brown biotite occurring predominantly near garnet porphyroblasts has up to 4.4 wt% TiO_2 and $X_{Fe} = 0.38$–0.43. Some inversely zoned plagioclase is only found in contact with garnet. EMP analyses of garnet, feldspar and biotite are given in Table S1. A modal analysis (4500 points counted) shows that the metapelite sample contains 18% garnet, 14% kyanite, 14% alkali feldspar, 21% biotite, 29% quartz, 2% plagioclase and about 2% accessories. This modal composition rich in garnet, kyanite, biotite, alkali feldspar and quartz points to a restitic metapelite.

Within one layer of the studied sample, aggregates of very fine exsolved mesoperthite (lamellae width 1–2 µm) with braid perthite texture occur (Fig. 1e). Locally, the mesoperthite recrystallized to an irregular intergrowth of alkali feldspar and plagioclase. EMP analyses (defocused beam, 5 µm, n = 48) on the finely exsolved mesoperthite yielded an integrated bulk composition of 27.9 ± 1.2 mol% albite, 62.1 ± 2.3 mol% orthoclase, 10.0 ± 1.1 mol% anorthite (Table S1).

The metapelite from a nearby locality is cross-cut by a leucocratic vein, which contains up to 2 cm-sized, deformed grains of antiperthite (width of lamellae and rods about 0.1–0.2 mm), orthoclase perthite and quartz ribbons in a fine-grained matrix of recrystallized feldspar and quartz. Reintegration of a large antiperthite grain (EMP analyses, n = 457) yields a bulk composition of 60% albite, 24% anorthite, 16% orthoclase components. The vein is affected by shearing oblique to the vein strike.

Characterization of garnet porphyroblasts and their inclusions

The garnet porphyroblasts are subhedral, and many show embayed, corroded margins, where the garnet breakdown product biotite (Fig. 1c) is associated with kyanite laths (length < 50 µm), plagioclase or mesoperthite (Fig. 1f). All these minerals are also found in < 50 µm wide veins crossing the porphyroblasts. Less corroded subhedral porphyroblasts show a typical chemical zonation with a grossular-rich core and a pyrope-rich mantle (Fig. 2a, Table S1). Towards the rim, where garnet is in contact with biotite, the pyrope component decreases again. Inversely to grossular, almandine contents increase from core to rim, especially at the outer rim in contact with biotite. Spessartine contents are slightly elevated (1–3 mol%) in the core. A similar but more pronounced zoning pattern is found in garnet, partially enclosed in a kyanite porphyroblast: in
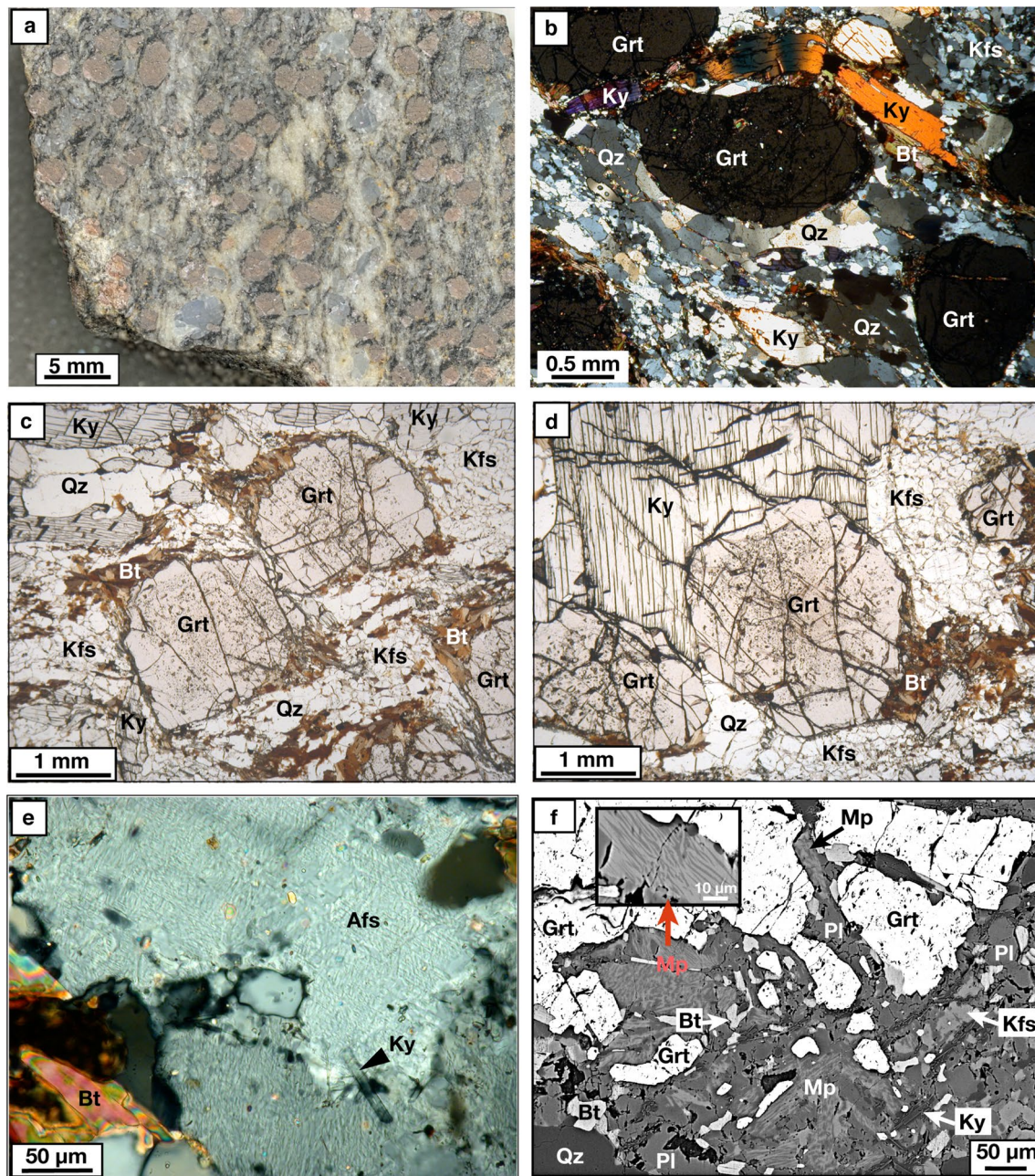
Fig. 1 Photo of hand specimen **a** and microphotographs of thin sections **b–e** of the investigated metapelite sample T70G. **a** Garnet (pink) rimmed by biotite (black) and coarse-grained bluish-grey kyanite in the quartz-feldspar matrix; **b** Quartz ribbon with subgrain texture and kyanite bent around garnet porphyroblasts in strongly deformed quartz-feldspar matrix (crossed polars); **c** Garnet porphyroblasts with fine-grained biotite at their grain boundaries in recrystallized quartz-feldspar matrix; **d** Garnet porphyroblast dispersed by small inclusions and partly enclosed by coarse-grained kyanite in recrystallized quartz-feldspar matrix; **e** Enlarged part of the fine-grained matrix showing biotite, alkali feldspar (mesoperthite) and tiny kyanite (crossed polars); **f** BSE image of a garnet porphyroblast corroded and replaced by mesoperthite (Mp), plagioclase, less biotite, kyanite and quartz. The inset shows an enlarged mesoperthite grain in contact with garnet. *Mineral abbreviations* according to Whitney and Evans (2010): *Ab* albite, *Afs* alkali feldspar, *Alm* almandine, *Als* aluminosilicate, *An* anorthite, *Bt* biotite, *Cc* calcite, *Dol* dolomite, *Grs* grossular, *Grt* garnet, *Ilm* ilmenite, *Kfs* K-feldspar, *Ky* kyanite, *L* liquid, *Mgs* magnesite, *Mp* mesoperthite, *Omp* omphacite, *Or* orthoclase, *Ph* phengite, *Pl* plagioclase, *Prp* pyrope, *Qz* quartz, *Rt* rutile, *Sil* sillimanite, *Sps* spessartine
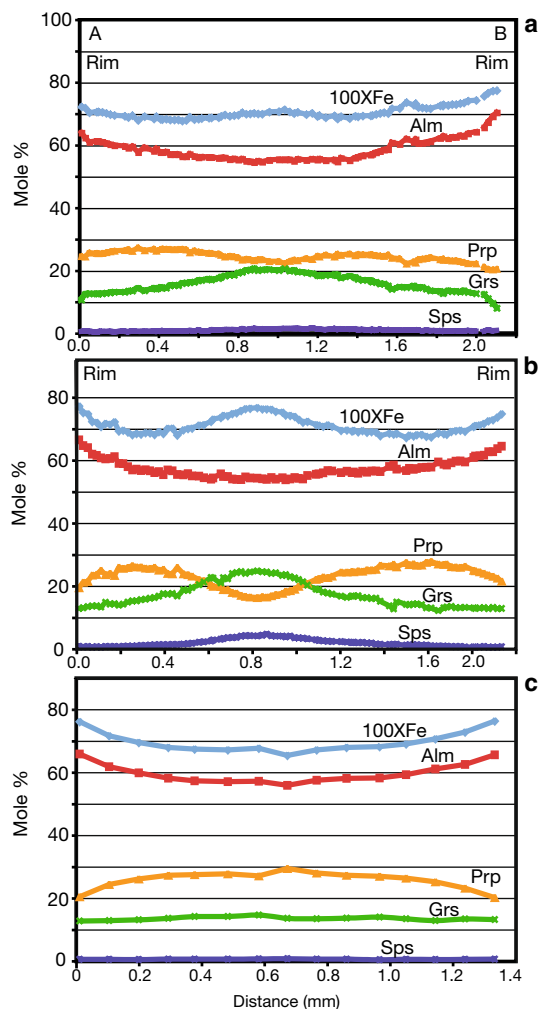
Fig. 2 Three compositional profiles (rim-core-rim) across garnet porphyroblasts displaying different types of zoning: **a** typical zoning pattern of a garnet porphyroblast shown in a Mg mapping image (profile A–B in Fig. 5a); **b** bell-shaped zoning profile with a spessartine-rich core from garnet partly enclosed in quartz and in a kyanite porphyroblast; **c** garnet showing only a retrograde zoning pattern with increasing x_{Fe} towards the rim

the garnet core spessartine and grossular contents increase to 6 and 26 mol%, respectively (Fig. 2b). Other garnet grains in contact with biotite miss a similar core but display increasing X_{Fe} at the rim (Fig. 2c).

A great variety of inclusions are interspersed throughout the garnet porphyroblasts (Fig. 3a). The identification and characterization of the inclusions is based on EMP analyses with backscatter electron images (BSE) and micro-Raman spectroscopy. The predominant inclusions are quartz, besides biotite, antiperthitic plagioclase, rutile, dolomite, calcite, kyanite, graphite, apatite, zircon and monazite, ranging in size from about 1 to 100 µm. Besides monomineralic inclusions, also bimineralic, polymineralic and fluid inclusions occur. Some of the inclusions show strikingly

well-developed negative crystal shapes orientated parallel to the garnet crystallographic structure (Fig. 3b).

Polymineralic inclusions

The studied polymineralic inclusions in the garnet porphyroblasts are up to 60 µm in diameter and located at some distance from the late veins described above and their Mg-depleted and Fe-enriched contact zones. Only some inclusions display a thin halo about 5 µm wide, slightly depleted in grossular component by about 2 mol% and/or enriched in almandine component by about 2 mol%. Two main types of polymineralic inclusions can be distinguished:

Type I—silicate-dominated inclusions consist of quartz, plagioclase, biotite, kyanite, dolomite (≤ 10 vol%), and accessory zircon, monazite, apatite, rutile, titanite. Type I inclusions have a mean size of 30 µm and their shape varies from euhedral to subhedral negative crystal shape (Fig. 4a–d). Frequent offshoots (Fig. 4a, b), similar to structures of decrepitated fluid inclusions make them distinct from the mono- and bimineralic inclusions. The silicate-dominated inclusions occur in a broad pyrope-rich mantle zone (Fig. 5a, b).

Type II—carbonate-rich inclusions consist of dolomite (13–42 vol%), quartz (20–47 vol%), kyanite (12–48 vol%) and rare allanite and Zn-bearing spinel (the volume fraction has been determined from BSE images). Type II inclusions are the most frequent type and have a mean size of 20 µm. The shape of the Type II inclusions varies from negative crystal shape to irregular shapes, however, offshoots have not been observed (Fig. 6a–c). These inclusions are found next to Type I inclusions (Fig. 5b) but some also occur in the garnet core.

Silicate-dominated Type I inclusions show a unique granoblastic texture of plagioclase and quartz with straight grain boundaries and an equilibrium angle of about 120° (Fig. 4a, b). The garnet-inclusion interfaces show reentrant angles at junctions of interface boundaries of plagioclase, quartz and biotite (Fig. 4a, b). The shape of biotite varies from subhedral to anhedral. Generally, kyanite occurs as tiny euhedral blades (Ky2 in Fig. 4c). Kyanite with subhedral and largely embayed shape (Ky1 in Fig. 4c), similar to kyanite in the matrix, is seldom and probably represents a trapped mineral like euhedral and subhedral crystals of rutile, apatite and zircon. In some of the Type I inclusions, plagioclase, biotite and kyanite appear to be arranged in contact with the garnet host, whereas quartz is located in the center of the inclusion (Fig. 4d).

Plagioclase and biotite inside Type I inclusions have a distinctly different composition compared to the rock matrix (Table S3). Plagioclase shows high and variable anorthite (An) contents (mostly 50–70, rarely 90 mol% An), in contrast to the lower An content in the rock matrix (30–40 mol%
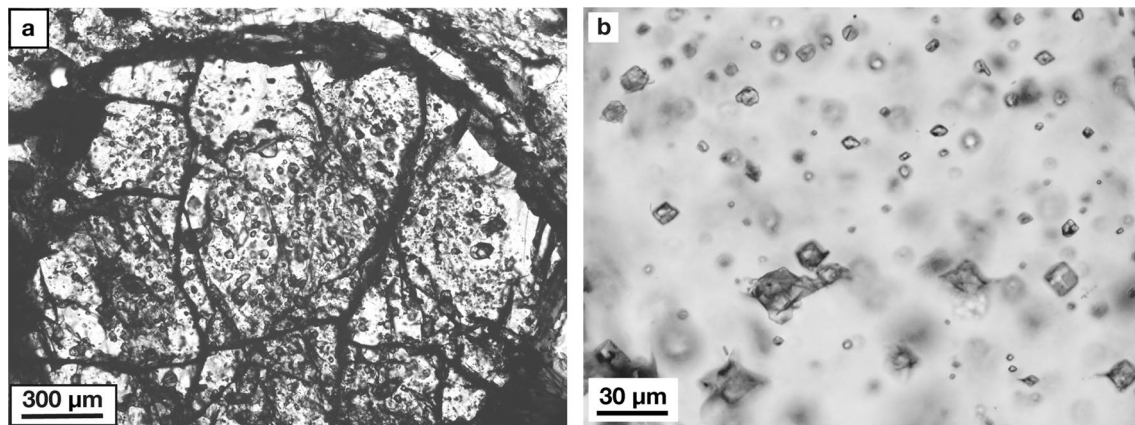
Fig. 3 **a** Photomicrographs (transmitted light) of inclusions (monomineralic, polymineralic and fluid inclusions) interspersed in a euhedral garnet porphyroblast (120 μm thick section). **b** Cluster of inclusions showing well-developed negative crystal shapes with parallel crystallographic orientation

Fig. 4 BSE images of silicate-rich polymineralic inclusions (Type I) in garnet with typical slightly varying mineral phases. **a**, **b** Inclusions with offshoots and in **a** with a granoblastic texture of plagioclase and quartz with straight grain boundaries and an equilibrium angle of about 120°. The garnet-inclusion interface shows reentrant angles > 120° at junctions of interface boundaries of plagioclase, quartz and biotite (white arrows). **c** Inclusion with two kyanite generations, the older one with subhedral, embayed shapes, the younger one is represented by tiny euhedral kyanite blades. Dolomite content typically is below 10 vol%, euhedral rutile is accessory. **d** Inclusion with negative crystal shape. Mineral abbreviations according to Fig. 1
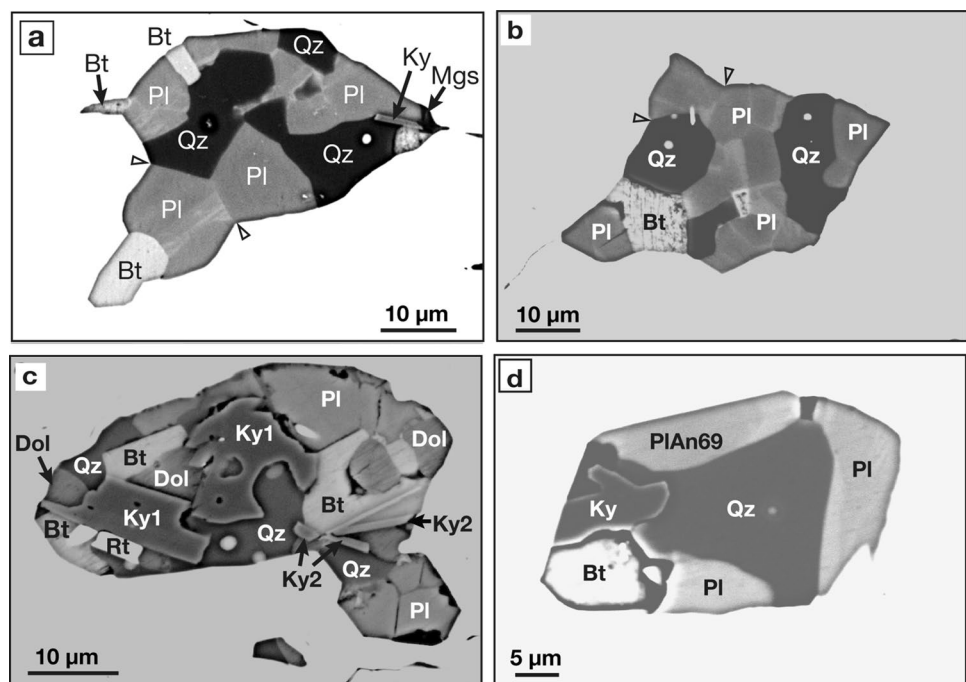
An). Biotite in Type I inclusions is much lower in X_{Fe} (about 0.25) and lower in Ti (0.28 cations p.f.u.) compared to the matrix biotite ($X_{Fe} = 0.38$–0.43, Ti $= 0.38$–0.48 cations p.f.u). Carbonate is predominantly dolomite, as in the rock matrix.

In the carbonate-rich Type II inclusions, dolomite is also the main carbonate mineral and only rarely magnesite, calcite, siderite and ankerite have been found as additional phases. The shape of dolomite and quartz is anhedral whereas kyanite often forms distinct euhedral blades (Fig. 6), but may also show skeletal shapes (Figs. 6c, 11c). The same mineral assemblage but with a different texture inside Type II inclusions was identified by Micro-Raman 2D spectral mapping (Fig. 7). They show a negative crystal shape and the enclosed minerals are tightly intergrown (Fig. 7c, d). In one of these inclusions a CO_2 fluid (≤ 5 vol%) with a density of 0.79 g/cm^3 was detected by Micro-Raman spectrometry.

All crystals identified as aluminum silicate by EMP analysis in both inclusion types have been confirmed as kyanite by Raman analyses. Corroded crystals as well as tiny euhedral blades within the polymineralic inclusions are kyanite, irrespective where the inclusions are situated inside the garnet porphyroblasts. Kyanite has also been confirmed in the recrystallized rock matrix.

Fig. 5 EDS X-rays element distribution maps for Mg of zoned garnet porphyroblasts **a**, **b** showing the location of the silicate-rich polymineralic inclusions (red circles) and carbonate-rich inclusions (yellow circles); **b** silicate and carbonate-rich inclusions occur together in the Mg-rich growth zone. *Grt* garnet, *Bt* biotite
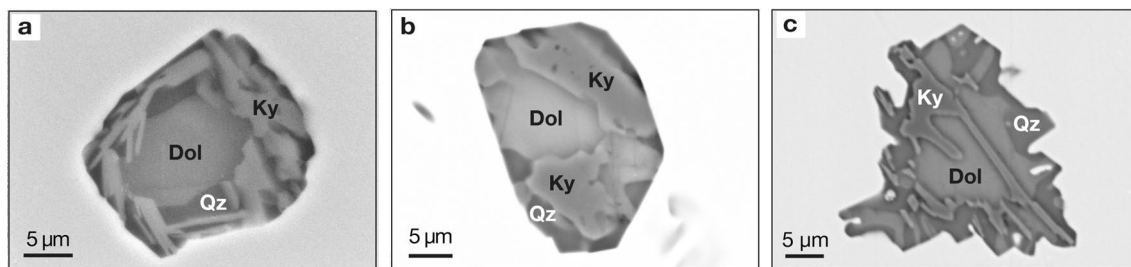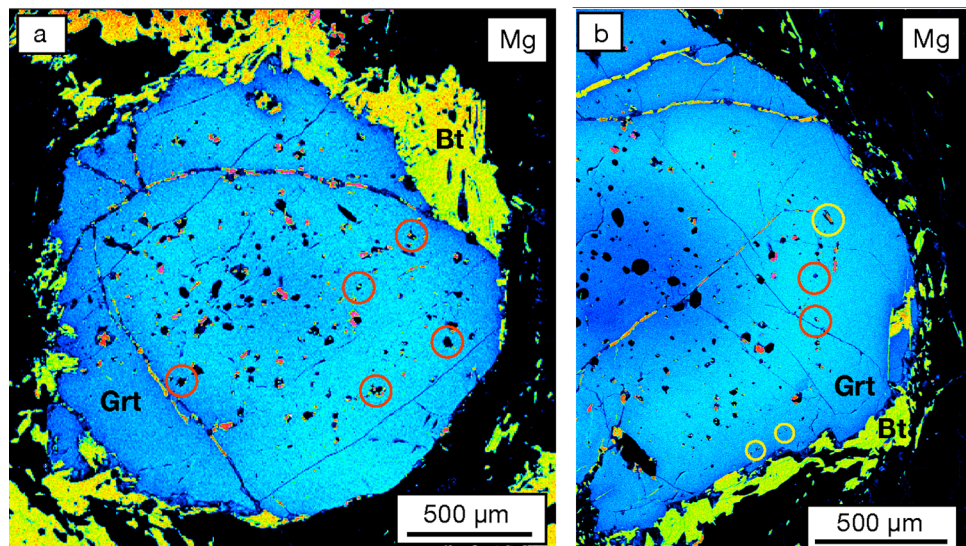

Fig. 6 BSE images of carbonate-rich polymineralic inclusions (Type II) in garnet. Inclusions with dolomite (> 10 vol%), quartz, kyanite show negative crystal shape **a**, **b** but also irregular shapes occur **c**. *Dol* dolomite, *Qz* quartz, *Ky* kyanite

Carbon-dominated inclusions

Fluid inclusions occur side by side with polymineralic inclusions. Most fluid inclusions appear in small groups, have euhedral negative crystal shape and their size is < 10 μm (Fig. 8a). Another type of fluid inclusions, irregular or elongated in shape, appears in healed cracks or surround silicate-rich inclusions in halos or marks radial cracks (Fig. 8b). In some CO_2–N_2 inclusions, solid phases of carbonate (siderite or dolomite) and/or traces of pyrophyllite at the inclusion rim have been found (Fig. 9). The composition as determined by Micro-Raman analyses, is similar for both inclusion types and dominated by CO_2 with variable proportions of N_2 (up to 7 mol%, Table S2). As accidentally trapped minerals within CO_2 inclusions, zircon, quartz and brookite were identified by Micro-Raman analyses. H_2O was not detected in the fluid phase.

CO_2 density (Table S2) was calculated according to the method based on the distance (Δ) between the Fermi diad (two highest intensity Raman bands, see Fall et al. 2011). However, for Δ-values greater than 105.5 (Table S2, marked with asterisks) the densimeter of Fall et al. (2011)

is not calibrated. Densities resulting from calibrated Δ-values ≤ 105.5 only, vary in the range 1.04–0.64 g/cm^3 without a clear correlation to one of the two inclusion types. However, higher densities (e.g. 1.11–1.12 g/cm^3) calculated from not calibrated Δ values > 105.5 (Table S2) match with previously determined fluid inclusion densities from the same metapelite sample, determined by microthermometry (Herms 2002). These densities of CO_2 fluid inclusions analysed in garnet are calculated from the homogenization temperatures using the data of Angus et al. (1976) and yield similar high densities of about 1.11 g/cm^3.

Graphite only occurs in garnet porphyroblasts, either as single euhedral or rounded inclusions (Fig. 8c), but never as lamellae, with a size between 3 and 10 μm or as composite inclusions of graphite + CO_2, or graphite + dolomite + CO_2 ± N_2 (Fig. 8d). The distribution of the graphite inclusions is irregular, but in many places they cluster around polymineralic carbonate-dominated inclusions. As the Raman spectrum of carbonaceous material is sensitive to its crystallinity, ordered and disordered structures can be distinguished (e.g. Wopenka and Pasteris 1993). Most of the analysed graphite inclusions show a perfectly ordered
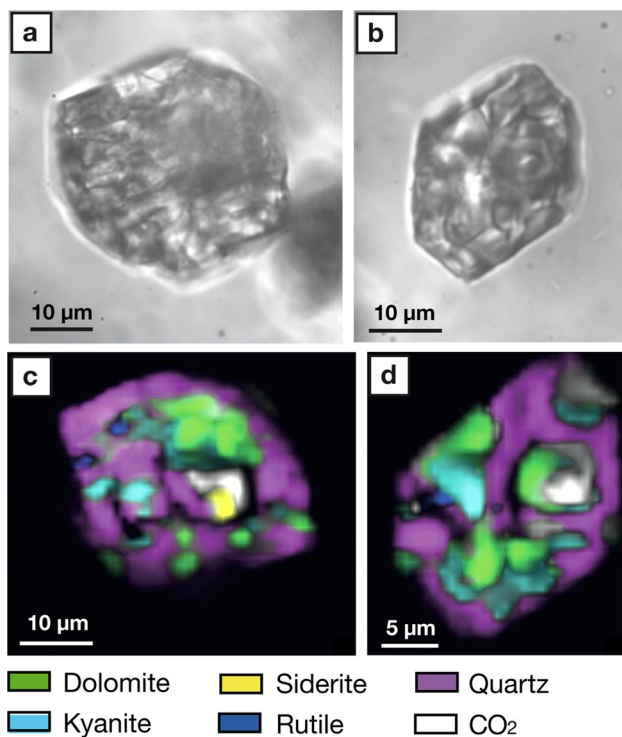
Fig. 7 **a**, **b** Photomicrographs of carbonate-rich polymineralic inclusions in garnet with negative crystal shape. **c**, **d** Their Raman 2D spectral images show the intense intergrowth of the mineral phases and the occurrence of CO_2 ($\rho = 0.79$ g/cm^3)

structure (Fig. S5a), graphite with slightly disordered structure is rare. In contrast, graphite enclosed in CO_2 inclusions is disordered according to their Micro-Raman peaks (Fig. S5b).

Rare earth element geochemistry of carbonate-rich inclusions

The analyses of REE and Sr allow to distinguish the origin of the carbonate-rich inclusions as either carbonatitic melts or as reaction product between garnet and CO_2 fluid. In-situ LA–ICP–MS analyses were performed on dolomites of carbonate-rich polymineralic inclusions with the highest volume fraction of the dolomite phase. Due to the correction method and for comparison with the dolomite spectra, the garnet host in contact with the polymineralic inclusions has also been analysed. The Sr content in dolomite is low, but slightly higher than in the garnet host, where Sr is mostly below the detection limit (Table S3). The REE content and the chondrite-normalized REE spectra show a higher concentration of LREE in dolomite (Fig. 10a) compared to garnet (Fig. 10b), while the MREE and HREE contents are in a similar range for dolomite and garnet. Very striking for dolomite is the positive slope of the LREE towards the MREE, a very similar trend compared to the garnet spectra. The

correction procedure of the analyses (see Chapter "Methods") constrains that the REE concentrations are indeed related to dolomite and are not mixed with the host garnet composition.

Remelting experiments

High P–T remelting experiments are a means to obtain direct information on the composition of the melt, trapped as polymineralic inclusions in the garnet porphyroblasts (Bartoli et al. 2013). After experimental rehomogenization, the inclusions are quenched to glass and can be subsequently analysed by EMP. Successful remelting of the silicate-rich polymineralic inclusions at high pressure and temperature conditions (most of them with a size < 20 μm) also verifies that these inclusions do not represent aggregates but originate from trapped melts that subsequently crystallized. As water was not added to the sample capsules for the experimental run, the melt formation in the inclusions is only a result of melting of the inclusion minerals.

The P–T conditions of the experiments were based on the peak metamorphic conditions (1.5–1.9 GPa, 750–800 °C) reported by Möller et al. (1995), Brown et al. (2020), and Tamblyn et al. (2021). These P–T conditions, mostly based on classic geothermobarometry, are suspected to be too low as discussed later (see "Discussion"). For the first set of rehomogenization experiments in a piston cylinder apparatus, the minimum pressure of 1.5 GPa was selected while temperatures of 750, 850 and 900 °C were used at equal run times of 24 h. At the lowest temperature of 750 °C, more than 80% of the silicate-rich inclusions show no signs of melt formation. Few glass inclusions are interspersed with needle-shaped aluminum silicate formed during quenching of the melt. At 850 °C, inclusions could not be analysed, as observable inclusions at the polished sample surface are lacking. At 900 °C, silicate-rich inclusions show either partial melting in the interspace between rounded crystals of quartz, plagioclase, biotite or kyanite (Fig. 11a) or complete melting, yielding a glass with newly formed aluminum silicate needles (Fig. 11b). Quite common is the appearance of a small bubble (5–10 vol%), which can be a shrinkage bubble or the result of incomplete dissolution of the fluid into the melt phase (Ferrero et al. 2018; Carvalho et al. 2019). However, it was not possible to detect volatiles or solid phases by Raman analyses in these bubbles. Some contacts between inclusion and host garnet are sometimes saw-tooth like (Fig. 11b), and a very thin but sharply bounded reaction rim between garnet and melt developed. The composition of this reaction rim, presumably formed by dissolution and re-precipitation, exhibits lower grossular and higher pyrope contents than the host garnet. The carbonate-rich inclusions show no melting, but partially decompose with resulting voids (Fig. 11c). However, reactions within the inclusions
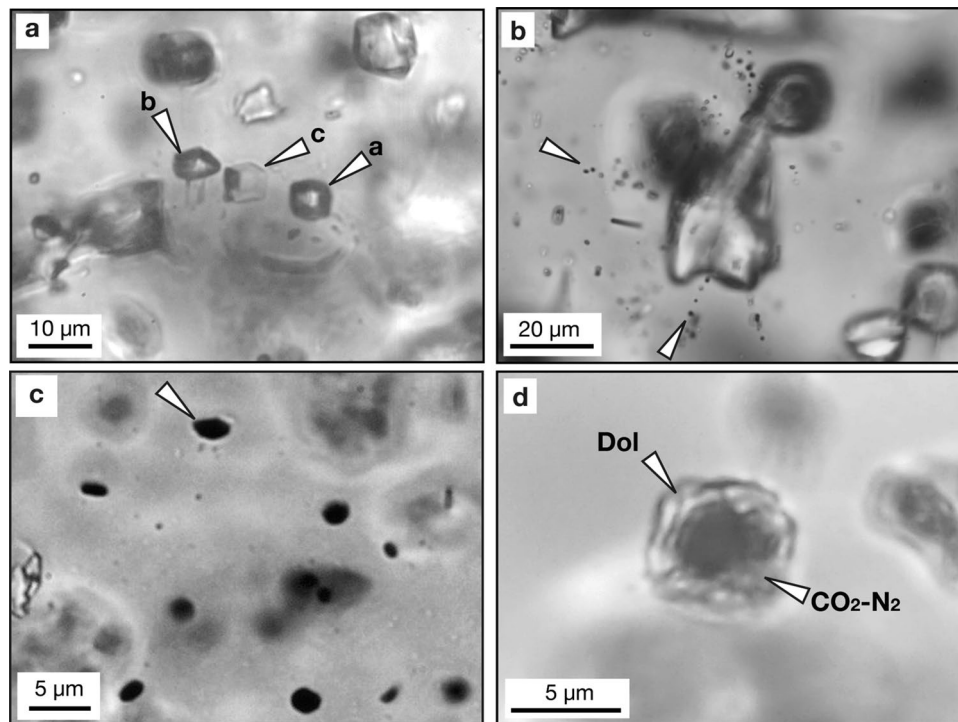
Fig. 8 **a** CO_2–N_2 fluid inclusions (*a, b*) with pyrophyllite (*a*: $N_2 = 0.28$ mol%, $\rho > 1.081^*$ g/cm³: *b*: $N_2 = 0.64$ mol%, $\rho > 1.081^*$ g/cm³), showing similar Raman spectra (Fig. 9) but without siderite; *c*: dolomite with attached CO_2–N_2 fluid inclusion ($N_2 = 3.4$ mol%, $\rho = 0.64$ g/cm³). **b** Fluid inclusions radiating from a decrepitated polymineralic silicate-rich inclusion. One analyzed inclusion with CO_2–N_2 ($N_2 = 0.76$ mol%, $\rho = 0.84$ g/cm³) contains siderite and

pyrophyllite (see spectrum Fig. 9). *The ρ-values with asterics are higher than the maximum calibrated value 1.081 g/cm³ for the 105.5 Fermi splitting with Fall et al. (2011). **c** Euhedral graphite inclusions in a cluster of carbonate-rich polymineralic inclusions. Graphite with arrow shows a well-ordered Raman spectrum (Fig. S5a). **d** Composite cuboid inclusion of well-ordered graphite surrounded by dolomite and CO_2–N_2 fluid. *Dol* dolomite

Fig. 9 Representative Raman spectra of the fluid inclusion (Fig. 8d) containing CO_2-N_2, siderite and pyrophyllite
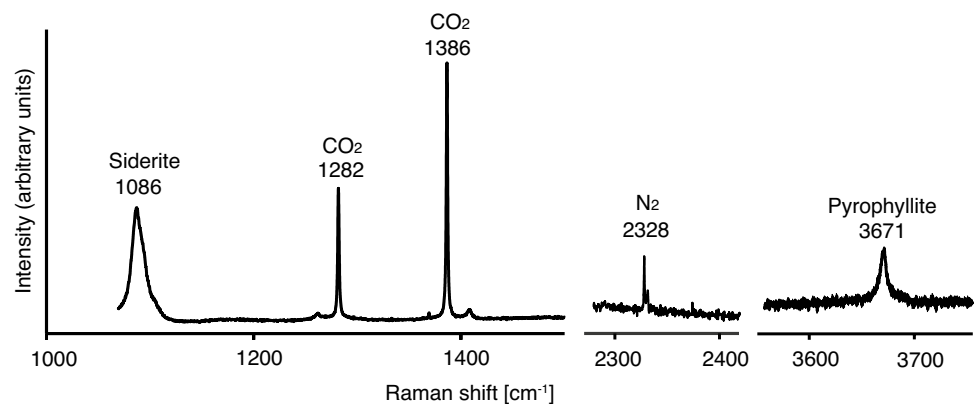
must also have taken place, because new minerals (pyroxenes and pyrope-rich garnet) formed in some cases.

The second set of rehomogenization experiments was conducted at a much higher pressure of 2.5 GPa and at higher temperatures of 950, 1000 and 1050 °C, to ensure successful remelting. At 1000 °C, in a time series with 6, 24 and 48 h run duration no signs of incipient melting were observed at 6 h, whereas at 48 h reaction of the garnet host with the melt is evidenced by new mineral formation, e.g.

orthopyroxene. All runs at 2.5 GPa and 24 h run time lack bubbles inside the remelted glass inclusions (Fig. 11d). This confirms that the inclusions at these conditions were completely rehomogenized (Ferrero et al. 2018; Carvalho et al. 2019). The bubble formation observed in experiments performed at lower pressures is interpreted as incomplete dissolution of the fluid into the melt phase. At 950 °C, no completely remelted inclusions have been observed, while the highest percentage of completely rehomogenized inclusions
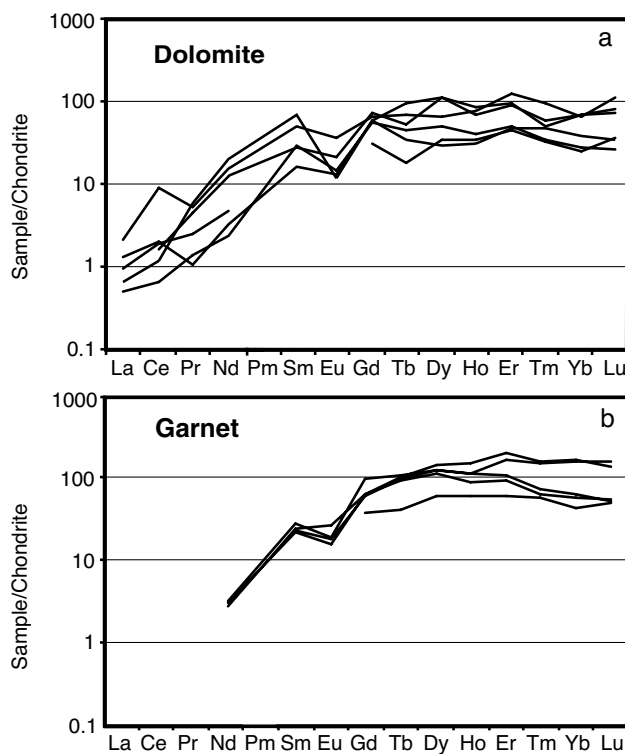
Fig. 10 A Chondrite-normalized (Boynton 1984) REE pattern of dolomite in the carbonate-rich inclusions and **b** of the host garnet surrounding the carbonate-rich inclusions

(Fig. 11d, e) was obtained at 1000 and 1050 °C, and a run time of 24 h. However, some homogenized glass inclusions show a halo of pyrope-rich garnet (Fig. 11f) at these experimental conditions. This indicates that some reaction of the melt with the garnet host occurred. Based on EMP element mapping, only inclusions that did not show melt inhomogeneities, halos or other reaction products (Fig. 11d, e), and thus confirm no modification of the melt composition during the experiments were selected to determine the bulk composition of the primary melt.

Bulk composition of the rehomogenized melt inclusions

Sixteen microprobe analyses on glassy inclusions without any obvious modification of the melt composition during the experiments have been selected (Table S4). In order to get information on the type of melt produced during anatexis of the metapelitic rock at high temperatures and pressures, the melt composition of the selected polymineralic inclusions are plotted in different diagrams: In the TAS diagram (total alkali versus silica) after Le Bas et al. (1986) the melt composition (H_2O- and CO_2-free basis) plots in the rhyolite field according to the IUGS classification for volcanic rocks (Fig. S6a). The mean melt composition is about 9 wt% total

alkali and 72 wt% silica. In the Ab–An–Or diagram after Barker (1979), the melt compositions fall in a relatively narrow range in the Or-rich part of the granite field at relatively high An-contents (Fig. S6b, Table S4). The mean composition in terms of feldspar components in the melt in wt% with standard deviation is: $29.3 \pm 5.3\%$ Ab, $62.8 \pm 4.8\%$ Or, $7.9 \pm 2.3\%$ An. The limited compositional range confirms that the silicate-rich polymineralic inclusions are not mineral aggregates accidentally captured during garnet growth but represent truly trapped melts. The mean melt composition in wt% (calculated without fluid components) is as follows: 71.65% SiO_2, 0.35% TiO_2, 16.03% Al_2O_3, 1.70% FeO, 0.04% MnO, 0.31% MgO, 0.99% CaO, 2.22% Na_2O, 6.69% K_2O. The melt is especially rich in K_2O with a high K_2O/($Na_2O + Na_2O$) ratio of 0.75. Figure S6c shows that there is a linear relation between the alkalinity index (AI) and the alumina saturation index (ASI) and that the melts plot in the peraluminous field.

Thermodynamic modelling

For thermodynamic modelling of the equilibrium phase diagram for the studied metapelite sample, the H_2O and CO_2 contents must be considered. Since the H_2O content has not been analysed, it was estimated by different methods: (1) Assuming H_2O saturated conditions, a H_2O content of 0.94 wt% is estimated from the mean of 15 EMP analyses of biotite (4.7 wt% H_2O neglecting possible F and Cl contents) and from the modal content of biotite in the rock (20 vol%) obtained from point counting. (2) A H_2O content of less than 1.3 wt% is derived from several calculations of the equilibrium phase assemblages assuming different H_2O contents in the rock: the observed subsolidus assemblage Grt + Bt + Pl + Afs + Ky + Qz is only stable at about 1 wt% H_2O. At higher contents, phengite should be present which has not been found, not even in trace amounts. The presence of some CO_2 is indicated only by CO_2 fluid inclusions observed in garnet, kyanite and quartz, and by traces of late retrograde carbonate. Since the CO_2 content of the rock cannot be estimated, it has been neglected in the calculation of the phase diagrams (Figs. 12, 13).

The equilibrium phase diagrams show the subsolidus field (green), a stability field for the recrystallized subsolidus assemblage Grt + Bt + Pl + Afs + Ky + Qz (dark green), two narrow yellow-shaded fields just above the solidus, with the assemblage Grt + Ph + Afs + Ky + Qz + Rt $\pm$ Bt and the suprasolidus fields above the phengite-out line (light red). Above 1.0 GPa and 770 °C, melting starts by complete breakdown of phengitic mica. Above 1.4 GPa and 800 °C, continuous phengite breakdown takes place in a narrow temperature field (yellow-shaded area in Fig. 12) that widens to about 20 °C with increasing pressure. During this breakdown reaction, the melt volume increases to about 10 to 15%. After
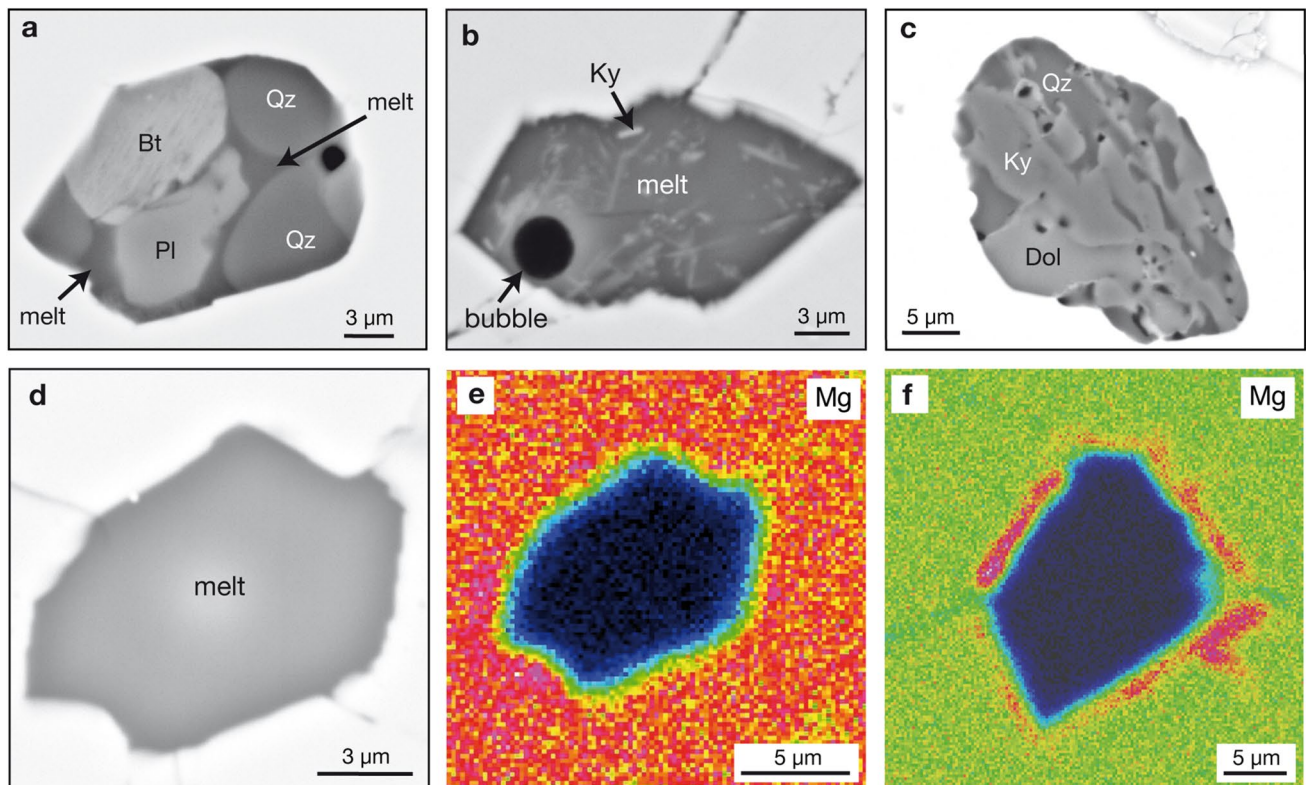
Fig. 11 Experimental products of rehomogenization experiments at 1.5 GPa, 900 °C, 24 h: **a** silicate-rich inclusion with interstitial partial melt between rounded mineral phases; **b** silicate-rich inclusion with a higher percentage of melt, with crystallization of secondary kyanite and a bubble; **c** carbonate-rich inclusion with no indication of melting, but with distinct porosity.—Experimental products of rehomog- enization experiments at 2.5 GPa, 24 h: **d** completely homogenized silicate-rich inclusion remelted at 1050 °C. **e** The Mg distribution map documents no reaction rim between glass inclusion and garnet host at 1050 °C. **f** The Mg distribution map shows a reaction rim of a newly precipitated pyrope-rich garnet around a homogenized glass inclusion at 1050 °C. Mineral abbreviations see Fig. 1

phengite breakdown, the melt volume further increases with increasing temperature, especially where biotite decomposes at pressures below 1.8 GPa. The primary mineral assemblage observed in the restitic metapelite (Grt + Rt + Afs + Ky + Qz) obviously coexisted with melt at temperatures above 900 °C.

Discussion

Implications from polymineralic melt inclusions, fluid and graphite inclusions

Evidence for a CO_2 fluid

CO_2 fluid inclusions are the most obvious indications for the presence of a CO_2-rich fluid phase. Those inclusions appearing in small groups with an euhedral negative crystal shape lying next to polymineralic inclusions (Fig. 8a) can be regarded as primary formations. Fluid inclusions irregular or elongated in shape occurring in healed cracks or surrounding silicate-rich inclusions in halos or marking radial

cracks (Fig. 8b) can be interpreted as secondary formations. Their formation can be correlated with the crystallization of the melt inclusions (at about 0.9 GPa, 750 °C), thereby liberating the CO_2, which was dissolved in the melt before. Some crystallizing melt inclusions decrepitated due to the overpressure and, e.g. a CO_2 fluid inclusion halo or radial cracks could form (Fig. 8b).

The densities of primary and secondary fluid inclusions are relatively similar, and could be explained by re-equilibration of the primary inclusions at similar P–T conditions at which the secondary fluid inclusions formed. The joint presence of polymineralic silicate-rich, former melt inclusions, carbonate-rich inclusions and CO_2 fluid inclusions suggests, that partial melting must have occurred in the presence of a CO_2 fluid phase (Carvalho et al. 2023 and references therein). The melt inclusions probably formed during phengite breakdown when melt developed over a short temperature interval, while the CO_2 fluid inclusions could have been enclosed in the garnet already in the green stability fields (Fig. 12). However, CO_2 fluid inclusions could also have become enclosed in
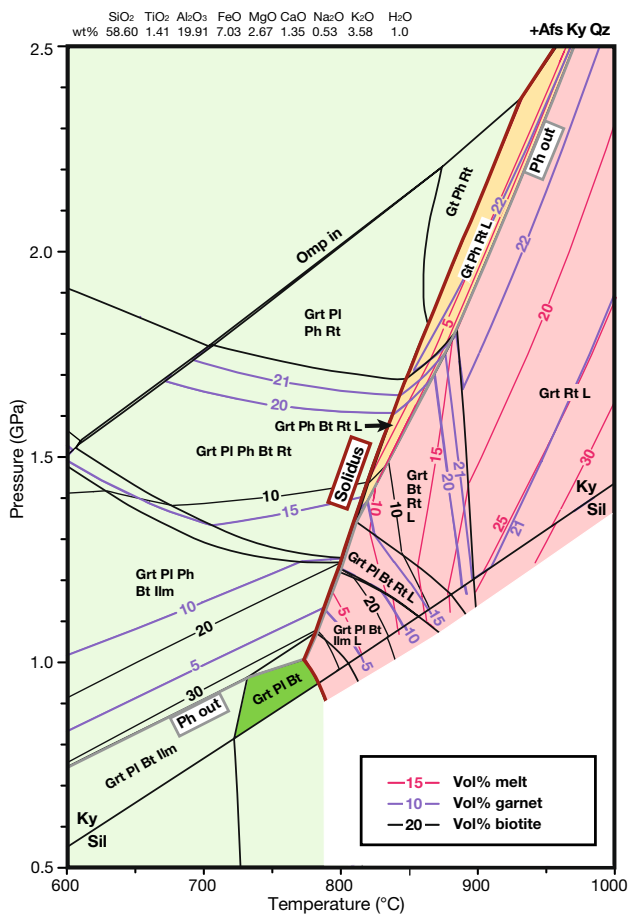
Fig. 12 Equilibrium phase diagram calculated for the metapelite T70G with an estimated content of 1 wt% H_2O. The subsolidus stability fields are shaded in light green, the suprasolidus fields are shaded in pink. Isopleths for vol% garnet, biotite and melt are plotted. The melt volume isopleths are most dense in the narrow fields (yellow color) where phengite decomposes to form melt. At pressures below 1 GPa, the phengite-out boundary (Ph out) is very near to the kyanite-sillimanite phase boundary. The dark green field marks the stability field of the assemblage $Grt + Pl + Bt + Afs + Ky + Qz$ present in rock matrix. Mineral abbreviations see Fig. 1
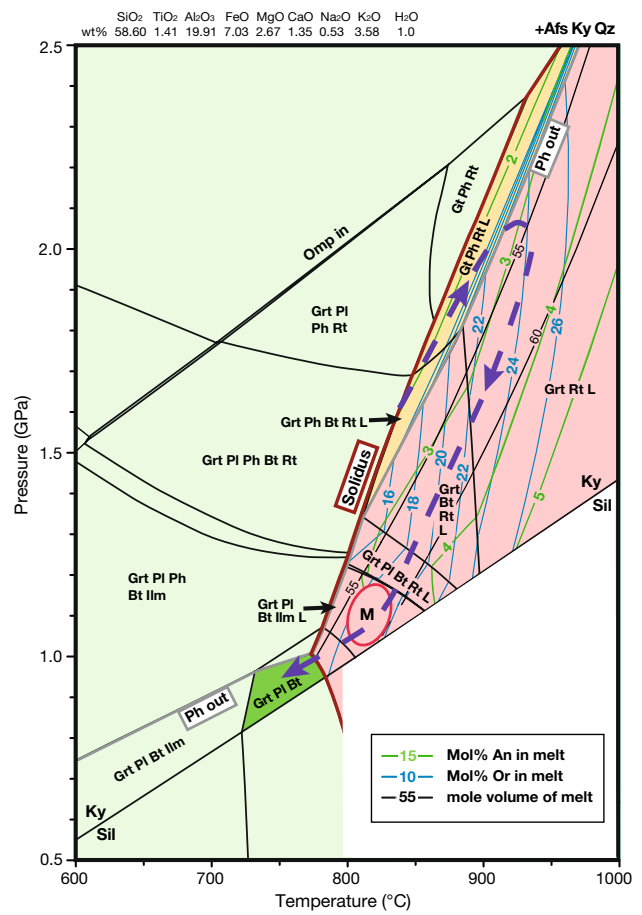
Fig. 13 Equilibrium phase diagram calculated for the metapelite T70G as in Fig. 12. Isopleths are plotted as indicated in the lower right inset. The melt inclusions should be entrapped in the upper part of the phengite decomposition field where the composition of the feldspar components in the melt coincide with those calculated by THERIAK. In the oval-shaped field M, the calculated composition of the melt coincides with the reintegrated composition of mesoperthite interpreted as metastable ternary feldspar formed from the last crystallized melt after fast decompression. The course of the P–T path (broken arrow) is discussed in the text. Mineral abbreviations see Fig. 1

garnet at the beginning of the phengite breakdown reaction, just before CO_2 was dissolved in the growing melt volume. The additional occurrence of variable amounts of N_2 in the CO_2 inclusions most probably has its source from biogenic material in the metasediments. Nitrogen is incorporated as NH_4^+ mainly in mica and feldspar (Honma and Itihara 1981; Harris et al. 2022) and will be released during breakdown of these minerals. The variable N_2 content of the CO_2 fluid inclusions over μm scales is interpreted to be due to in situ N_2 liberation from mica and thus excludes a pervasive homogeneous fluid flux. Although no H_2O has been found in the CO_2 fluid inclusions, the presence of some water is indicated by traces of pyrophyllite, as described as well, e.g. by Carvalho et al. (2019).

Pyrophyllite crystallized at the late retrograde stage at about 400 °C.

The process of partial melting most likely was initiated by liberation of H_2O due to mica breakdown reactions during heating, leading to dehydration melting (Vielzeuf and Holloway 1988; Patiño Douce and Harris 1998) in the presence of a CO_2 fluid phase. While a high amount of the liberated H_2O will be dissolved in the melt phase, only a small amount of CO_2 can be dissolved. The solubility of CO_2 in silicate melts is lower than that of H_2O but increases with pressure (Tamic et al. 2001). According to experiments by Duncan and Dasgupta (2014), 0.5–2.0 wt% CO_2 can be dissolved in rhyolitic melts at pressures of 1.5–2.0 GPa. The presence of ≤ 10 vol% dolomite in

the siliceous polymineralic inclusions further suggests that also CO_2 must have been dissolved in the former melt inclusions.

Graphite inclusions and the source of CO_2

As a source of CO_2, in-situ formation by oxidation of biogenic graphite to CO_2 has been proposed by Cesare et al. (2005), Barich et al. (2014), Tacchetto et al. (2018), Carvalho et al. (2019) and Ferrero et al. (2021) for migmatites and granulites. During progressive metamorphism, biogenic graphite develops a platy shape and is found in the rock matrix, within garnet, in nanogranite inclusions and in fluid inclusions as described by the latter authors. However, the graphite from Yalumba Hill neither occurs in the matrix of the metapelitic rocks, nor as a trapped mineral within polymineralic inclusions in garnet porphyroblasts, which means that graphite was not enclosed in garnet before the melt inclusions were trapped. Although a complete oxidation of biogenic graphite to CO_2 at an early stage cannot be excluded for Yalumba Hill, it is more likely that CO_2 originated from nearby marbles or calcsilicate rocks by reaction of carbonate with quartz or silicates. The liberated CO_2 has been trapped as well in the growing garnet, where graphite precipitated at the contact with the almandine-rich garnet host by CO_2 reduction through simultaneous oxidation of Fe^{2+} to Fe^{3+} of the garnet. Such a process of carbon reduction by local iron oxidation through reactions between the garnet host and a fluid phase has been described by Frezzotti et al. (2011), who detected halos of Fe^{3+}-enriched garnet around diamondiferous inclusions. Graphite precipitation from a fluid can occur at variable conditions and mechanisms as discussed in detail by Luque et al. (1998). However, in garnet porphyroblasts of Yalumba Hill single euhedral or rounded graphite inclusions occur together with exceptional composite cuboid inclusions of ordered graphite surrounded by dolomite and CO_2–N_2 fluid (Fig. 8d). Such composite inclusions have not been observed for biogenic graphite but have instead been described by Perraki et al. (2006) from the Rhodope UHP metamorphic province and were interpreted as precipitates from a CO_2 or C–O–H fluid.

An indication for a high-temperature formation of this graphite can be obtained from the ordering of the graphite structure, which is temperature dependent and can be deduced from the Raman spectra (Fig. S5a). Comparing the Raman spectra with the spectra published by Buseck and Beyssac (2014), based on the empirical geothermometer calibrated by Beyssac et al. (2002) up to 700 °C, a formation temperature of at least 700 °C can be deduced for the perfectly ordered graphite inside the garnet porphyroblasts in the Yalumba Hill eclogitic metapelite.

Carbonate-rich polymineralic inclusions

Two formation scenarios are considered for the carbonate-rich polymineralic inclusions: (1) crystallization of a carbonatitic melt or (2) reaction of the CO_2 fluid inclusion with the garnet host.

(1) Carbonate-rich polymineralic inclusions in garnet crystallized from a carbonatite-like melt have been described by Ferrero et al. (2016) from migmatites of the Bohemian Massif (Central Europe). Inclusions of anatectic carbonatites of crustal origin occur together with nanogranitic inclusions. Although highly variable, the REE are distinctly enriched in the calcite-rich inclusions compared to the silicate-rich inclusions and can reach values up to, e.g. 110 µg/g La (Ferrero et al. 2016).

We initially hypothesized that the carbonate-rich inclusions in garnet from Yalumba Hill could be enclosed carbonatitic melt. However, LREE concentrations (e.g. La ≤ 0.7 µg/g) even lower than the MREE and HREE contents (Fig. 10a, Table S3), indicate that this dolomite could not have been crystallized from a carbonatitic melt, generally containing La concentrations of about 100 to > 1000 µg/g (Deans and Powell 1968; Bell and Simonetti 1996). Similarly, the low Sr content (≤ 15.9 µg/g) compared to 1250 µg/g Sr in the carbonatite inclusions investigated by Ferrero et al. (2016) argues against a carbonatitic origin (general Sr content 1000 up to > 10,000 µg/g, Chakhmouradian et al. 2016). Carbonate-rich inclusions of carbonatitic origin in general show a significant enrichment of LREE and a negative slope of the spectra towards MREE. In striking contrast, dolomite in the carbonate-rich inclusions from Yalumba Hill shows a positive slope towards MREE, which contradicts an origin from carbonatitic melts.

(2) The mineral association Dol + Ky + Qz invariably observed in the carbonate-rich inclusions could have formed by reaction of CO_2 with the garnet host (Tacchetto et al. 2018; Carvalho et al. 2020), although other, relatively small CO_2 fluid inclusions in garnet are well preserved and obviously did not react with the garnet, probably on kinetic reasons. During that reaction, garnet is replaced by dolomite, quartz and kyanite. While the latter two minerals cannot incorporate REE, dolomite obviously inherited the typical REE spectrum of garnet with its positive trend (Fig. 10a, b). The fact that carbonates can inherit the HREE elements during replacement of garnet by Mg calcite, has also been reported by Korsakov and Hermann (2006). An equilibrium phase diagram calculated with THERIAK-DOMINO for a composition combining 1 mol CO_2 with 5 mol of host garnet shows the stability limit of garnet in contact with CO_2 (Fig. 14). During cooling garnet breaks down in a narrow stability field to the assemblage kyanite + quartz + carbonate until CO_2 is completely consumed. A BSE image of a typical carbonaceous inclusion displaying that assemblage without
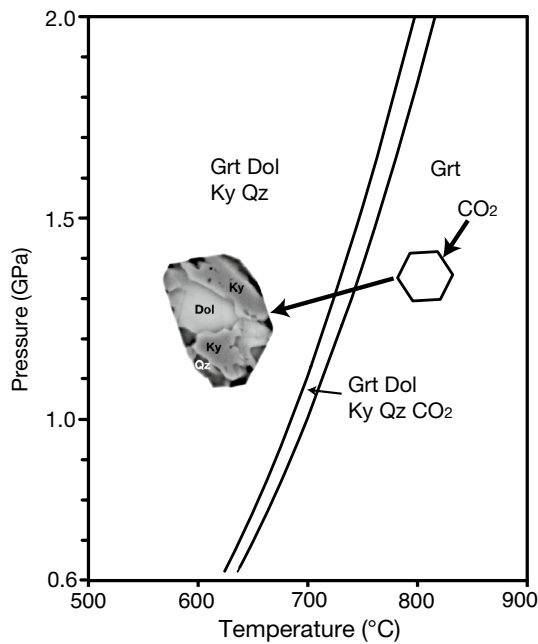
Fig. 14 Equilibrium phase diagram calculated by THERIAK-DOMINO for host garnet (Gt6: composition given in Table S1) near carbonaceous inclusions combined with CO_2 fluid (5 mol Gt6 + 1 mol CO_2). The mineral assemblages formed by reaction of CO_2 fluid with the garnet host after temperature decrease is displayed in a BSE image. Mineral abbreviations see Fig. 1

any relict CO_2 is shown as inset in Fig. 14. According to EMS analyses (Table S1) the carbonate is dolomite with $X_{Fe} = 0.2$. Rarely, relics of CO_2 and traces of siderite have been detected by Raman spectroscopy (Fig. 7).

The hypothesis of former carbonate or carbonatite-like inclusions in garnet has also been tested by THERIAK-DOMINO modelling. However, the combination garnet + carbonate always results in quartz-free or even SiO_2-undersaturated assemblages, which were not observed in the sample. The quartz-bearing assemblage of the carbonate-rich polymineralic inclusions is thus a further argument for them originating from the reaction of garnet with a CO_2 fluid and not with a carbonatitic melt.

Implications for melt formation and P–T path

The P–T conditions of the experimental rehomogenization of the polymineralic inclusions (2.5 GPa, 1000–1050 °C) provide an upper limit of the trapping conditions of the melt. A lower pressure limit of about 2 GPa can be derived from the discussion of the earlier works by Möller et al. (1995) and Tamblyn et al. (2021). According to Möller et al. (1995), eclogites and metapelites from Yalumba Hill underwent pressures of 1.5–1.9 GPa and temperatures of 750–800 °C, determined by classic geothermobarometry. However, geothermometry based on Fe–Mg exchange might give

erroneous results, especially in high-grade metamorphic rocks, because the Fe and Mg contents could be changed after peak metamorphism by diffusion inside the mineral grains and between different minerals. Therefore, the estimated peak-metamorphic temperatures derived from Fe–Mg exchange thermometry on garnet–biotite, garnet–hornblende and garnet–clinopyroxene pairs in metapelites and metabasites from Yalumba Hill by Möller et al. (1995) could have been significantly higher. Tamblyn et al. (2021) report results from Zr-in-rutile thermometry for rutile inclusions in garnet in retrogressed eclogites from about the same locality. The rutile inclusions appear to reflect a prograde history from about 600 to 800 °C. The peak-metamorphic pressure of 1.8 GPa derived from GASP barometry was interpreted by Möller et al. (1995) as a minimum pressure, because the K-feldspar content in plagioclase has not been considered. Similarly, the pressure derived from the reaction albite = jadeite + quartz (Holland 1980, 1990) should be a minimum value, if the exsolved jadeite component in clinopyroxene is not considered (P > 1.8 Gpa, Möller et al. 1995). In addition, those two geobarometers would give even higher pressures when calculated for higher temperatures. A possible temperature of 900 °C would yield pressures of at least 2 GPa. This is supported by a temperature of 900 °C obtained by feldspar thermometry (Fuhrman and Lindsley 1988) on cm-large antiperthite grains in a leucosome vein from a nearby locality (result of this study, see "Petrography"). Furthermore, according to thermodynamic modelling, the inferred peak assemblage garnet + omphacite + rutile + quartz in metabasites from the Usagaran belt (Yalumba) is stable above 1.8 GPa (Figs. 10–12 in Tamblyn et al. 2021). In conclusion, the peak-metamorphic P–T conditions of at least 2.0 GPa and 900 °C are considered as realistic.

In order to derive more information on the P–T conditions of entrapment of the melt inclusion, the composition of the rehomogenized melt inclusions is compared with the melt composition calculated by THERIAK for different pressures and temperatures. Inside the narrow P–T fields (yellow in Figs. 12, 13), where the phengite dehydration melting reaction takes place, the calculated normative feldspar components in the melt inclusions (CIPW norm, Table S4) are closely consistent with those calculated by THERIAK (2.1 ± 0.9 mol% An, 8.6 ± 2.0 mol% Ab, 17.0 ± 1.4 mol% Or, with 2σ standard deviation). In Fig. 13, the isopleths for 2% An and 16–18% Or plot inside that field and are about parallel above 1.5 GPa. Therefore, the melt inclusions could have been trapped anywhere between 1.5 and 2.5 GPa inside the narrow dehydration melting field of phengite.

The melt inclusions probably would be entrapped when relatively fast melting occurs, i.e. in the phengite dehydration field and only during garnet growth. This is only possible for a steep prograde P–T path within the dehydration

melting field oblique to the reaction boundaries. In the P–T range 1.5–2.0 GPa, the garnet volume increases from 17 to 22 vol%. In view of the steep P–T path, which may suggest a fast subduction, disequilibrium growth of garnet might be considered. Although it is generally accepted that the transport of elements through the rock matrix towards the growing garnet porphyroblast is limiting its growth rate, element transport at very high temperatures of metamorphism and in the presence of melt can be significantly faster. On the other hand, diffusion inside the garnet porphyroblasts, in spite of high temperatures might be too slow to allow equilibration with the rock matrix except at the garnet edge. In this case, the garnet core is out of equilibrium. Therefore, for modelling the equilibrium phase relations, the garnet core should be subtracted from the bulk rock composition. This leads to a rather high percentage of newly grown garnet, depending on the P–T conditions and on the percentage of garnet core volume subtracted. If, for instance, 90 vol% of the garnet porphyroblasts in the restitic metapelite from Yalumba Hill with the composition calculated with THERIAK at 1.6 GPa and 840 °C is subtracted from the bulk rock composition, about 16–18 vol% of newly grown garnet should be formed. More realistically, a continuous process considering diffusion velocities inside and outside the garnet porphyroblasts at the specific metamorphic conditions has to be taken into account, but exploring this is outside the scope of this paper. In any case, the growth of garnet up to high pressures and temperatures, where melt inclusions could be entrapped, should be possible.

A large amount of melt produced at temperatures higher than 900 °C should have triggered the subsequent fast uplift. A steep uplift and cooling path with exhuming and cooling rates of 0.06–0.22 GPa/Ma and 20–25 °C/Ma, respectively, based on the $^{207}Pb/^{206}Pb$ monazite age interpreted as peak-metamorphic growth age and a $^{207}Pb/^{206}Pb$ titanite age interpreted as cooling age, has been reported by Möller et al. (1995) and Collins et al. (2004). As shown in Fig. 13, such a path will run nearly parallel to the isopleths for constant mole volume of the melt, meaning that no overpressure will develop inside the melt inclusions so that they will neither decrepitate nor implode at this stage. Following this steep path down to lower pressures, the stability field of Grt + Bt + Rt + Afs + Ky + Qz + L is attained and the biotite content increases at the expense of garnet (shown by the isopleths in Fig. 12), consistent with the observation of garnet corrosion features. The same reaction features were described by Indares and Dunning (2001) in similar high P–T metapelites from the Tshenukutish terrane, Grenville Province. At about 1.3 GPa, plagioclase observed at the rim of garnet porphyroblasts would have crystallized at the expense of the grossular component of garnet and the albite component of the melt. Both reactions did not achieve equilibrium conditions since the volume contents of garnet, plagioclase and biotite do not

correspond to volume contents calculated by THERIAK for equilibrium conditions, although the reactions occur in the presence of melt. The garnet breakdown reactions appear to have been blocked by the simultaneous crystallization of kyanite and quartz locally at the rim of garnet (Fig. 1b, d). Moreover, ilmenite that should have formed at the expense of rutile, has only been detected locally at the margin of rutile, further supporting a fast uplift path.

A fast uplift path is consistent with the preservation of prograde zoning in garnet (Fig. 2a, b). Although it is well known that diffusion at higher temperature can eliminate prograde zoning in garnet (e.g. Caddick et al. 2010; Schwarzenbach et al. 2021; Devoir et al. 2021) the upper temperature limit (about 800 °C) for a preservation of element zoning is dependant on several factors like garnet size, fluid activity, length of peak metamorphic conditions and exhumation rate. There are, however, even high- and ultra-high temperature rocks, e.g. the Saxonian Granulitgebirge (O'Brien and Rötzler 2003), the Moldanubian Zone, Austria (Cooke et al. 2000) or the Gruf Complex (Galli et al. 2011), where a prograde garnet zoning has been preserved despite metamorphic peak temperatures of > 900 °C. In this study a short retention time at high temperature together with rapid exhumation and cooling have to be assumed. Galli et al. (2011) could document by intra-crystalline diffusion modelling that the garnet zoning profile is preserved when the UHT metamorphic event is brief enough (< 20 Ma) and post-UHT cooling is rapid. A fast uplift path is furthermore consistent with the observation of the finely exsolved mesoperthite (Fig. 1e, f), which occurs interstitially in the rock matrix beside perthite with much lower albite component. The integrated composition of the mesoperthite with 28.4 mol% Ab, 10.3 mol% An, and 61.3 mol% Or (Table S1) is in strong contrast to the equilibrium composition of the alkali feldspar calculated with THERIAK. This calculated composition is in the range 13–15 mol% Ab, 1–2 mol% An and 83–85 mol% Or in the stability field of the assemblage Grt + Pl + Bt + Ilm + Afs + Ky + Qz + L. The mesoperthite is interpreted as metastable ternary feldspar, later exsolved, which crystallized in disequilibrium due to rapid decompression and cooling with the composition of the feldspar components in the melt. This hypothesis is corroborated by the fact that in a restricted P–T field (M in Fig. 13), the integrated composition of the mesoperthite coincides within σ standard deviation with the composition of the feldspar components in the melt—30 mol% Ab, 9.5 mol% An and 60.5 mol% Or—calculated by THERIAK and normalized to 100%. Metastable ternary feldspar with the composition of the melt with respect to An, Ab, Or components has, to our knowledge, never been reported before in metamorphic rocks. Considering a steep P–T path parallel to the isolines for the mole volume of melt, the question arises how to explain the offshoots of the polymineralic inclusions,

which imply an internal overpressure. In fact, because of the pressure dependence of CO_2 solubility in silicate melts (Tamic et al. 2001), CO_2 will be exsolved at lower pressures. This will produce an overpressure in the inclusions that may result in the formation of offshoots and of secondary CO_2 fluid inclusions in the garnet host (Fig. 8b). These fluid inclusions as well as the modified primary CO_2 fluid inclusions have similar highest densities about 1.1 g/cm^3, compatible with pressures of around 0.9 GPa at temperatures of about 800 °C (Herms 2002).

At about these conditions, the P–T path should become shallower with both temperature and pressure decreasing. Since neither sillimanite nor phengite has been detected in the studied metapelite, the course of the P–T path is rather clearly defined going at about 780 °C and 0.9 GPa into the narrow subsolidus stability field of Grt + Pl + Bt + Afs + Ky + Qz (dark green in Fig. 13). During this stage, biotite and alkali feldspar recrystallized in the rock matrix (Fig. 1b–d) but no low-grade retrogression of the rock is observed, probably because of water-deficiency. Furthermore, some relatively large polymineralic inclusions appear to have recrystallized and equilibrated with the garnet host, judged from granoblastic textures between quartz and feldspar with reentrant angles in garnet (Fig. 4a, b). In summary, the 2 Ga old oceanic rocks from the Yalumba Hill, Usagaran belt, probably experienced steep and fast subduction and subsequent uplift at high temperatures. Fast uplift stalled at about 1.0–0.8 GPa entering midcrustal levels (Brown et al. 2020). A similar path, although at cooler conditions, is reported for oceanic rocks from the Lago di Cignana, Western Alps (Groppo et al. 2009).

Conclusions

Our investigation of polymineralic inclusions in garnet porphyroblasts of a restitic metapelite from the Usagaran belt provides evidence for partial melting of deeply subducted oceanic crustal rocks under high P–T conditions. Due to the deficiency of H_2O, there is little low-temperature overprint and the high-temperature assemblage garnet, kyanite, alkali feldspar, quartz and rutile is largely preserved. Melt inclusions, later crystallized to polymineralic inclusions, probably were trapped during phengite dehydration melting at high pressure and temperature. Remelting experiments on the polymineralic inclusions, containing plagioclase, quartz, biotite and kyanite yield a rhyolitic, peraluminous melt composition at 2.5 GPa and 1000–1050 °C. Beside silicate-rich polymineralic inclusions, dolomite-quartz-kyanite inclusions were found, which are interpreted as contemporaneously trapped inclusions. Extremely low LREE contents of the dolomite exclude a carbonatitic origin but favours an adoption of MREE and HREE contents from host garnet. Thermodynamic modelling supports a reaction of CO_2 with garnet leading to the formation of dolomite, quartz and kyanite. The CO_2 fluid most likely originated from decarbonation processes of intercalated carbonate rocks. A CO_2 production by oxidation of graphite is improbable because the rock matrix and the trapped polycrystalline inclusions in garnet are completely graphite-free. The CO_2 dominance is in striking contrast to most eclogite-facies subducted oceanic rocks, even those with metapelitic composition, where H_2O-rich fluid inclusions dominate (Table 1 in Frezzotti and Ferrando, 2015). At high pressures, the CO_2 fluid could be completely dissolved in the partial melt together with H_2O liberated from phengite breakdown.

On the basis of the remelting experiments, thermodynamic modelling and geothermobarometry from the literature (Möller et al. 1995; Brown et al. 2020; Tamblyn et al. 2021), minimum P–T conditions of 2.0 GPa and 900 °C for the peak of metamorphism are derived. However, because of the survival of Mn and Ca growth zoning of garnet, the peak stage of metamorphism must have been very short. The subsequent uplift should have been fast and probably along a steep path suggested from results of radiometric dating (Möller et al. 1995; Collins et al. 2004) and from the presence of metastable ternary alkali feldspar, crystallized with the composition of the feldspar components in the melt at about 1.1 GPa and 820 °C. Fast uplift through the mantle stalled at about 0.9–1.0 GPa, probably when the subducted material entered the lower crust. Below the solidus at 0.9 GPa and 770 °C, the metapelite crystallized with the assemblage garnet, biotite, plagioclase, alkali feldspar, kyanite and quartz.

Our investigation on one of the oldest oceanic crustal rocks supports the notion that plate tectonics and subduction processes were already active at 2 Ga. Exceptional for subducted oceanic crustal rocks are the high temperatures, which are in accordance with hotter conditions within the upper mantle 2 billion years ago. The HT eclogite-facies rocks from Yalumba Hill represent the rare case where partial melting of oceanic crustal rocks took place.

Data availability The data that support the findings of this study are available from the author (Petra Herms) upon reasonable request.

Declarations

Conflict of interest The authors have no competing interest to declare that are relevant to the content of this article.

References

Angus A, Armstrong B, de Reuk KM, Altuin VV, Gadetskii OG, Chapela GA, Rowlinson JS (1976) Carbon dioxide Vol. 3 of international thermodynamic tables of the fluid state. Pergamon Press, Oxford, p 385

Baldwin JA, Powell R, Brown M, Moraes R, Fuck RA (2005) Modelling of mineral equilibria in ultrahigh-temperature metamorphic rocks from the Anápolis-Itaucu Complex, central Brazil. J Metamorph Geol 23:511–531

Barich A, Acosta-Vigil A, Garrido CJ, Cesare B, Tajčmanová L, Bartoli O (2014) Microstructures and petrology of melt inclusions in the anatectic sequence of Jubrique (Betic Cordillera, S. Spain): implications for crustal anatexis. Lithos 206–207:303–320

Barker F (1979) Trondhjemites: definition, environment and hypotheses of origin. In: Baker F (ed) Trondhjemites, dacites, and related rocks. Elsevier, Amsterdam, pp 1–12

Bartoli O, Cesare B, Poli S, Acosta-Vigil A, Esposito R, Turina A, Bodnar RJ, Angel RJ, Hunter J (2013) Nanogranite inclusions in migmatitic garnet: behavior during piston-cylinder remelting experiments. Geofluids 13:405–420

Bartoli O, Acosta-Vigil A, Tajčmanová L, Cesare B, Bodnar RJ (2016) Using nanogranitoids and phase equilibria modeling to unravel anatexis in the crustal footwall of the Ronda peridotites (Betic Cordillera, S. Spain). Lithos 256–257:282–299

Bell K, Simonetti A (1996) Carbonatite magmatism and plume activity: implications from the Nd, Pb and Sr isotope systematics of Oldoinyo Lengai. J Petrol 37:1321–1339

Beyssac O, Goffé B, Chopin C, Rouzaud JN (2002) Raman spectra of carbonaceous material in metasediments: a new geothermometer. J Metamorph Geol 20:859–871

Boniface N, Tsujimori T (2019) Pillow lava basalts with back-arc MORB affinity from the Usagaran Belt, Tanzania: relics of Orosirian ophiolites. J Geological Soc 176:1007–1021

Boniface N, Tsujimori T (2021) New tectonic model and division of the Ubendian-Usagaran Belt, Tanzania: a review and in-situ dating of eclogites. In: Wakabayashi J, Dilek Y (eds) Plate tectonics, ophiolites, and societal significance of geology: a celebration of the career of eldridge moores: geological society of america special paper 552:133–175. https://doi.org/10.1130/2021.2552(08)

Boynton WV (1984) Geochemistry of the rare earth elements: meteorite studies. In: Henderson P (ed) Rare earth element geochemistry. Elsevier, Amsterdam, pp 63–114

Brown DA, Tamblyn R, Hand M, Morrissey LJ (2020) Thermobarometric constraints on burial and exhumation of 2-billion-year-old eclogites and their metapelitic hosts. Precambrian Res 347:105833

Buseck PR, Beyssac O (2014) From organic matter to graphite: graphitization. Elements 10(6):421–426. https://doi.org/10.2113/gselements.10.6.421

Caddick MJ, Konopásek J, Thompson AB (2010) Preservation of garnet growth zoning and the duration of prograde metamorphism. J Petrol 51:2327–2347

Carvalho BB, Bartoli O, Ferri F, Cesare B, Ferrero S, Remusat I, Capizzi IS, Poli S (2019) Anatexis and fluid regime of the deep continental crust: new clues from melt and fluid inclusions in metapelitic migmatites from Ivrea zone (NW Italy). J Metamorph Geol 37:951–975

Carvalho BB, Bartoli O, Cesare B, Tacchetto T, Gianola O, Ferri F, Szabó C (2020) Primary CO_2-bearing fluid inclusions in granulitic garnet usually do not survive. Earth Planet Sci Lett 536:116170

Carvalho BB, Bartoli O, Cesare B (2023) C-O–H fluid-melt-rock interaction in graphitic granulites and problems of quantifying carbon budget in the lower continental crust. Chem Geol 631:121503

Cesare B, Meli S, Nodari L, Russo U (2005) Fe^{3+} reduction during biotite melting in graphitic metapelites: another origin of CO_2 in granulites. Contrib Mineral Petrol 149:129–140

Cesare B, Ferrero S, Salvioli-Mariani E, Pedron D, Cavallo A (2009) Nanogranite and glassy inclusions: the anatectic melt in migmatites and granulites. Geology 37:627–630

Cesare B, Acosta-Vigil A, Bartoli O, Ferrero S (2015) What can we learn from melt inclusions in migmatites and granulites? Lithos 239:186–216

Chakhmouradian AR, Reguir EP, Couëslan C (2016) Calcite and dolomite in intrusive carbonatites. II. Trace-element variations. Miner Petrol 110:361–377

Coggon R, Holland T (2002) Mixing properties of phengitic micas and revised garnet-phengite thermobarometers. J Metamorph Geol 20(7):683–696

Collins AS, Reddy SM, Buchan C, Mruma A (2004) Temporal constraints on *Palaeoproterozoic eclogite* formation and exhumation (Usagaran Orogen, Tanzania). Earth Planet Sci Lett 224(1–2):175–192

Cooke RA, O'Brien PJ, Carswell DA (2000) Garnet zoning and the identification of equilibrium mineral compositions in high-pressure-temperature granulites from the Moldanubian Zone, Austria. J Metamorph Geol 18:551–569

De Capitani C, Petrakakis K (2010) The computation of equilibrium assemblage diagrams with Theriak/Domino software. Am Mineral 95(7):1006–1016

Deans T, Powell JL (1968) Trace elements and strontium isotopes in carbonatites, fluorites and limestones from India and Pakistan. Nature 218:750–752

Deng L-P, Liu Yi-C G-F, Groppo C, Rolfo F (2018) Partial melting of ultrahigh-pressure metamorphic rocks at convergent continental margins: evidences, melt compositions and physical effects. Geosci Front 9:1229–1242

Devoir A, Bloch E, Müntener O (2021) Residence time of igneous garnet in Si-rich magmatic systems: Insights from diffusion modeling of major and trace elements. Earth Planet Sci Lett 560:116771

Duncan MS, Dasgupta R (2014) CO_2 solubility and speciation in rhyolitic sediment partial melts at 1.5–3.0 GPa—implications for carbon flux in subduction zones. Geochim Cosmochim Acta 124:328–347

Fall A, Tattitch B, Bodnar RJ (2011) Combined microthermometric and Raman spectroscopic technique to determine the salinity of H_2O-CO_2-NaCl fluid inclusions based on clathrate melting. Geochim Cosmochim Acta 75:951–964

Ferrando S, Frezzotti ML, Dallai L, Compagnoni R (2005) Multiphase solid inclusions in UHP rocks (Su-Lu, China): remnants of supercritical silicate-rich aqueous fluids released during continental subduction. Chem Geol 223:68–81

Ferrero S, Bartoli O, Cesare B, Salvioli-Mariani E, Acosta-Vigil A, Cavallo A, Groppo C, Battiston S (2012) Microstructures of melt inclusions in anatectic metasedimentary rocks. J Metamorph Geol 30:303–322

Ferrero S, Braga R, Berkesi M, Cesare B, Laridhi Ouazaa N (2014) Production of metaluminous melt during fluid-present anatexis: an example from the *Maghrebian basement*, La Galite Archipelago, central Mediterranean. J Metamorph Geol 32:209–225

Ferrero S, Wunder B, Walczak K, O'Brien PJ, Ziemann MA (2015) Preserved near ultrahigh-pressure melt from continental crust subducted to mantle depths. Geology 43(5):447–450

Ferrero S, Wunder B, Ziemann MA, Wälle M, O'Brien PJ (2016) Carbonatitic and granitic melts produced under conditions of primary immiscibility during anatexis in the lower crust. Earth Planet Sci Lett 454:121–131

Ferrero S, O'Brien PJ, Borghini A, Wunder B, Wälle M, Günther C, Zieman MA (2018) A treasure chest full of nanogranitoids: An archive to investigate crustal melting in the Bohemian Massif. In: Ferrero S, Lanari P, Goncalves P, Grosch EG (eds) Metamorphic geology: microscale to mountain belts: geological society, vol 478. Special Publications, London, pp 13–38

Ferrero S, Ague JJ, O'Brian PJ, Wunder B, Remusat L, Ziemann MA, Axler J (2021) High pressure, halogen-bearing melt preserved in ultra-high temperature felsic granulites of the Central Maine Terrane, Connecticut (US). Am Mineral 106(8):1225–1236

Frezzotti ML, Selverstone J, Sharp ZD, Compagnoni R (2011) Carbonate dissolution during subduction revealed by diamond-bearing rocks from the Alps. Nat Geosci 4:703–706

Fuhrman ML, Lindsley DH (1988) Ternary feldspar modeling and thermometry. Am Mineral 73:201–215

Galli A, Le Bayon B, Schmidt MW, Burg J-P, Caddick MJ, Reusser E (2011) Granulites and charnockites of the Gruf Complex: evidence for Permian ultra high-temperature metamorphism in the Central Alps. Lithos 124:17–45

Gao X-Y, Chen Y-X, Zhang Q-Q (2017) Multiphase solid inclusions in ultrahigh-pressure metamorphic rocks: a snapshot of anatectic melts during continental collision. J Asian Earth Sci 145:192–204

Gervasoni F, Klemme S, Rohrbach A, Grützner T, Berndt J (2017) Experimental constraints on the stability of baddeleyite and zircon in carbonate- and silicate-carbonate melts. Am Mineral 102:860–866. https://doi.org/10.1016/j.lithos.2017.03.004

Gerya TV, Stoeckhert B, Perchuk AL (2002) Exhumation of high-pressure metamorphic rocks in a subduction channel – A numerical simulation. Tectonics 21(6):6-1-6–19. https://doi.org/10.1029/2002TC001406

Groppo C, Beltrando M, Compagnoni R (2009) The P-T path of the ultra-high pressure Lago Di Cignana and adjoining high-pressure meta-ophiolitic units: insights into the evolution of the subducting Tethyan slab. J Metamorph Geol 27:207–231

Grützner T, Kohn SC, Bromiley DW, Rohrbach A, Berndt J, Klemme S (2017) The storage capacity of fluorine in olivine and pyroxene under upper mantle conditions. Geochim Cosmochim Acta 208:160–170. https://doi.org/10.1016/j.gca.2017.03.043

Guillong M, Meier DL, Allan MM, Heinrich CA, Yardley BWD (2008) SILLS: a MATLAB-based program for the reduction of laser ablation ICP-MS data of homogeneous materials and inclusions. Miner Assoc Can Short Course 40:328–333

Harris BJR, de Hoog JCM, Halama R (2022) The behaviour of nitrogen during subduction of oceanic crust: insights from in situ SIMS analyses of high-pressure rocks. Geochim Cosmochim Acta 321:16–34

Hermann J, Rubatto D, Korsakov A, Shatsky VS (2001) Multiple zircon growth during fast exhumation of diamondiferous, deeply subducted continental crust (Kokchetav massif, Kazakhstan). Contrib Mineral Petrol 141:66–82

Herms P (2002) Fluids in a 2 Ga old subduction zone—deduced from eclogite-facies rocks of the Usagaran belt. Tanzania Eur J Mineral 14(2):361–373

Holland TJB (1980) The reaction albite = jadeite + quartz determined experimentally in the range 600–1200 °C. Am Mineral 65:129–134

Holland TJB (1990) Activities of components in omphacite solid solutions. Contrib Mineral Petrol 105:446–453

Holland TJB, Powell R (1998) An internally consistent thermodynamic data set for phases of petrological interest. J Metamorph Geol 16:309–343

Holland TJB, Powell R (2003) Activity–composition relations for phases in petrological calculations: an asymmetric multicomponent formulation. Contrib Mineral Petrol 145(4):492–501

Honma H, Itihara Y (1981) Distribution of ammonium in minerals of metamorphic and granitic rocks. Geochim Cosmochim Acta 45:983–988

Houketchang Bouyo M, Penaye J, Mouri H, Toteu SF (2019) Eclogite facies metabasites from the Paleoproterozoic Nyong Group, SW Cameroon: mineralogical evidence and implications for a high-pressure metamorphism related to a subduction zone at the NW margin of the Archean Congo craton. J Afr Earth Sc 149:215–234

Indares A, Dunning G (2001) Partial melting of high-P–T metapelites from the Tshenukutish Terrane (Grenville Province): petrography and U-Pb geochronology. J Petrol 42:1547–1565

Korsakov AV, Hermann J (2006) Silicate and carbonate melt inclusions associated with diamonds in deeply subducted carbonate rocks. Earth Planet Sci Lett 241:104–118

Labrousse L, Prouteau G, Ganzhorn AC (2011) Continental exhumation triggered by partial melting at ultrahigh pressure. Geology 39:1171–1174

Lafuente B, Downs RT, Yang H, Stone N (2016) The power of databases: the RRUFF project. In: Armbruster T, Danisi RM (eds) Highlights in mineralogical crystallography. De Gruyter O, Berlin, pp 1–30

Lang HM, Gilotti JA (2007) Partial melting of metapelites at ultrahigh-pressure conditions, Greenland Caledonides. J Metamorph Geol 25:129–147

Le Bas MJ, Le Maitre RW, Streckeisen A, Zanettin B (1986) A chemical classification of volcanic rocks based on the total alkali-silica diagram. J Petrol 27:745–750

Luque FJ, Pasteris JD, Wopenka B, Rodas M, Barrenechea JF (1998) Natural fluid-deposited graphite: mineralogical characteristics and mechanisms of formation. Amer J Sci 298:471–498

Maboko MA (2000) Nd and Sr isotopic investigation of the Archean-Proterozoic boundary in north-eastern Tanzania: constraints on the nature of Neoproterozoic tectonism in the Mozambique Belt. Precambrian Res 102(1–2):87–98

Meinhold K, Ott G (1993) Training course "Methods of regional geological mapping in Africa", explanatory notes on the 1:50.000 geological map of the Rudi area (Parts of sheets 180 and 198), Tanzania: Bundesanstalt für Geowissenschaften und Rohstoffe 111 011

Möller A, Appel P, Mezger K, Schenk V (1995) Evidence for a 2 Ga subduction zone: eclogites in the Usagaran belt Tanzania. Geology 23:1067–1070

Möller A, Mezger K, Schenk V (1998) Crustal age domains and the evolution of the continental crust in the Mozambique belt of

Tanzania: combined Sm-Nd, Rb-Sr, and Pb-Pb isotopic evidence. J Petrol 39:749–783

Newton RC, Charlu TV, Kleppa OJ (1980) Thermochemistry of the high structural state plagioclases. Geochim Cosmochim Acta 44:933–941

Ning W, Kusky T, Wang L, Huang B (2022) Archean eclogite-facies oceanic crust indicates modern-style plate tectonics. Proc Natl Acad Sci 119(15):e2117529119. https://doi.org/10.1073/pnas.2117529119

O'Brien PJ, Rötzler J (2003) High-pressure granulites: formation, recovery of peak conditions and implications for tectonics. J Metamorph Geol 21:3–20

Patiño Douce AE, Harris N (1998) Experimental constraints on Himalayan anatexis. J Petrol 39:689–710

Perraki M, Proyer A, Mposkos E, Kaindl R, Hoinkes G (2006) Raman micro-spectroscopy on diamond, graphite and other carbon polymorphs from the ultrahigh-pressure metamorphic Kimi Complex of the Rhodope Metamorphic Province, NE Greece. Earth Planet Sci Lett 241:672–685

Schwarzenbach EM, Zhong X, Caddick MJ, Schmalholz SM, Menneken M, Hecht L, John T (2021) On exhumation velocities of high-pressure units based on insights from chemical zoning in garnet (Tianshan, NW China). Earth Planet Sci Lett 570:117065

Stöckert B, Duyster J, Trepmann C, Massone HJ (2001) Microdiamond daughter crystals precipitated from supercritical COH + silicate fluids included in garnet, Erzgebirge, Germany. Geology 29:391–394

Tacchetto T, Bartoli O, Cesare B, Berkesi M, Aradi L, Dumond IE, Szabó C (2018) Multiphase inclusions in peritectic garnet from granulites of the Athabasca granulite terrane (Canada): evidence of carbon recycling during Neoarchean crustal melting. Chem Geol 508:197–209

Tajčmanová L, Connolly JAD, Cesare B (2009) A thermodynamic model for titanium and ferric iron solution in biotite. J Metamorph Geol 27:153–165

Tamblyn R, Brown D, Hand M, Morrissey L, Clark C, Anczkiewicz R (2021) The 2 Ga eclogites of Central Tanzania: directly linking age and metamorphism. Lithos 380–381:article 105890. https://doi.org/10.1016/j.lithos.2020.105890

Tamic N, Behrens H, Holtz F (2001) The solubility of H_2O and CO_2 in rhyolitic melts in equilibrium with a mixed CO_2-H_2O fluid phase. Chem Geol 174:333–347

Vielzeuf D, Holloway JR (1988) Experimental determination of the fluid-absent melting relations in the pelitic system. Contrib Mineral Petrol 98:257–276

White RW, Powell R, Holland TJB (2007) Progress relating to calculation of partial melting equilibria for metapelites. J Metamorph Geol 25(5):511–527

Whitney D, Evans B (2010) Abbreviations for names of rock-forming minerals. Am Mineral 95:185–187

Wopenka B, Pasteris JD (1993) Structural characterization of kerogens to granulite-facies graphite: applicability of Raman microprobe spectroscopy. Am Mineral 78:533–557